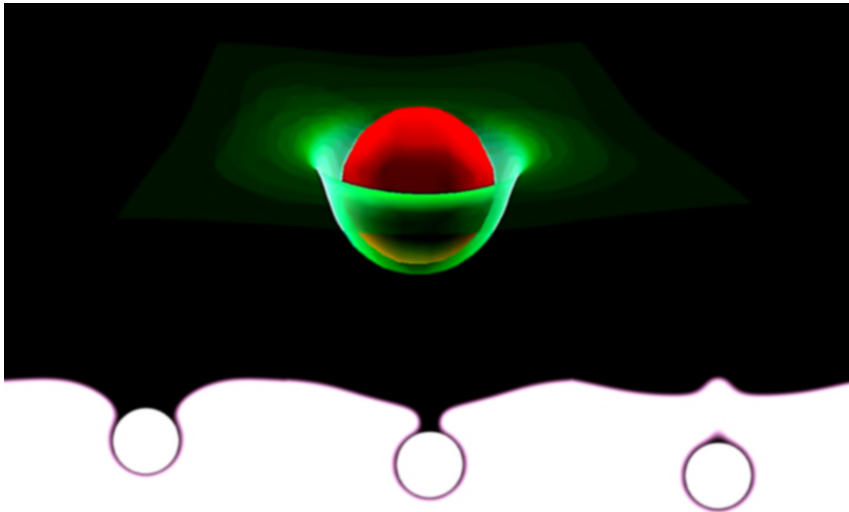Università degli Studi di Udine

Dottorato di Ricerca in
Scienze dell'Ingegneria Energetica e Ambientale
XXXV Ciclo - 2022

Particle interaction with binary-fluid interfaces

Fernando Kevin Miranda Santa Cruz

Author's e-mail:
 dokemir@gmail.com

Author's address:
 Dipartimento Politecnico di Ingegneria e Architettura
 Università degli Studi di Udine
 Via delle Scienze, 206
 33100 Udine – Italia
 office: +39 0432 558031

Cover picture:
 Sinking sphere: solid interaction with fluids interface.

Last update:
 Udine, March 10, 2023

Acknowledgments

Abstract

In this thesis, a computational tool has been developed to study multiphase interactions, more precisely ternary phase systems where a solid and a drop phase interact in a common incompressible Newtonian carrier fluid, considering the immersed solid phase properties (including wetting effects), the type of drops and the characteristics of the carrier fluid as controlling parameters. We use an Eulerian-Lagrangian methodology where the continuity and the Navier-Stokes equations are solved numerically by using a pseudo-spectral method for the carrier fluid. The drop phase is modelled by the Phase Field Method (PFM) and the solid phase is described using the Direct Forcing Immersed Boundary approach (DFIB) and inserted to the carrier fluid in the form of a virtual force. The approaches taken in this work consider the solid-fluid and fluid-drop interfaces as smooth transition layers represented by a continuous hyperbolic function. In order to generate a ternary phase system, the solid phase is coupled to the binary-fluid-phase by introducing a single well potential in the free-energy density functional, which can also control the solid surface wetting property. The implemented tool is proven to give reliable results in the studied applications, which are divided into three categories. The first one consists of a 2D and a 3D validation case study of a solid settling in a quiescent fluid. The second category shows solid interactions with a binary-fluid interface and the effects of surface wetting in the submergence of a quasi-buoyant body. Finally, the third category shows the equilibrium configuration of solid-drops pairs at different contact angles and the relative rotation of two solids (bridged by a drop), induced by shear fluid flow deformations on the drop's interface.

Contents

List of Figures

Dedication

This work is wholeheartedly and proudly dedicated to my parents, Fredy Miranda and Selinda Santa Cruz, whose unconditional and tireless support has always been a source of great strength for me, who had my back in many difficult situations and have always encouraged me to follow my dreams, helping me to make them come true. I also dedicate this thesis to my brother Fred, who is always my first choice for any technology advice and whose inventive ideas and creative mind will never stop surprising me.I also dedicate this dissertation to my beloved wife Hana, whose passion, determination, order and punctuality in whatever she does inspire me every day.

Nomenclature

Bo	Bond number
Ca	capillary number
Ch	Cahn number
$\mathcal{F}$	free-energy functional
$\boldsymbol{f}_{DF}$	virtual force
Fr	Froude number
FT	Front Tracking
h	characteristic length of the domain
h_{ss}	contact line position
I_{ss}	immersed solid volume portion
LBD	liquid bridged doublet
l_c	gravity-capillary waves characteristic length
LS	Level Set
$\mathcal{M}_\phi$	motility coefficient
μ_ϕ	chemical potential
P	pressure in the fluid domain
Pe_ϕ	phase field Péclet number
PFM	Phase Field Method
ϕ	phase field order parameter
ψ_s	fictitious solid phase field
Re	Reynolds number
Re_τ	shear Reynolds number
ρ_{fsub}	average fluid density
ρ_s	solid body density
t_c	gravity-capillary waves characteristic time
θ_{eq}	equilibrium contact angle
$\mathbf{u}$	velocity field
VoF	Volume of Fluid
We	Weber number
ξ	fluid interfacial layer thickness
ξ_s	solid interfacial layer thickness

1

Introduction

Solid-fluid-fluid interactions are ever-present in nature and in our everyday life. Early in the morning we come across self-assembled cereal clusters formed in our bowl of milk by lateral capillary forces (see fig. 1.1 (a)) [3, 4, 5]. Same forces play a crucial role in the life of water-walking creatures who rely on them to avoid drowning [6, 7]. When a raindrop falls into the sand, the grains attach to the drop surface (capillary bridge) by normal capillary forces as shown in fig. 1.1 (b) [8, 9]. We can also observe different behaviour of raindrops falling onto other surfaces, depending on the surface material, its curvature, its rigidity and its wettability.
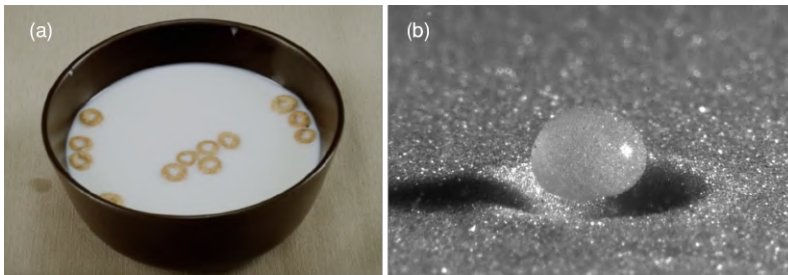
FIGURE 1.1 – (a) Self assembly of buoyant cereals on a free surface. (b) Raindrop covered with sand-grains after collision with the ground [1].

1.1 Mechanisms of interaction

Two important mechanisms are defined in the following subsections. The wetting effect — a general mechanism which controls the interactions of a solid surface and two fluids when they are brought into contact — and the capillary forces — the mechanism which becomes very important in the interaction among several individual wettable solid surfaces mediated by a fluid.

1.1.1 Wetting

Wetting is the ability of a liquid to cover a solid surface when the liquid and the solid are brought into contact. The degree of wetting is determined by the nature of the

fluids and the solid surface involved (Adhesive and cohesive forces balance).
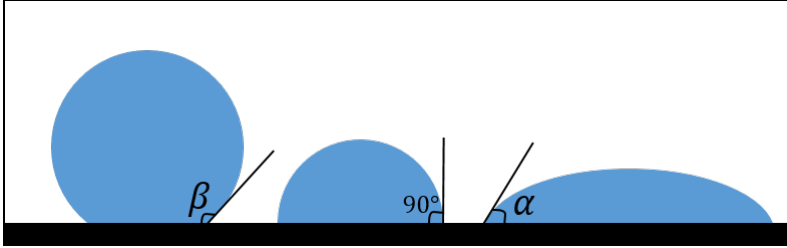
FIGURE 1.2 – Three cases of wettability are illustrated, where $\beta > 90°$ shows low wettability, $90°$ is neutrally wettable and $\alpha < 90°$ shows high wettability.

Contact angle and adhesive-cohesive forces

The contact angle θ is the angle measured from the solid surface to the fluid tangent line at the triple point (refer to fig. 1.2). Adhesive forces cause spreading of the liquid over the solid, decreasing thus the contact angle. On the other hand, cohesive forces tend to avoid the solid surface and they round up the liquid, causing big contact angles. The term hydrophobic surface refers to contact angles between $90° - 150°$ (surface with angles greater than $150°$ is called superhydrophobic), hydrophilic surface refers to contact angles between $0° - 90°$ and neutrally wettable surface refers to contact angles of $90°$.

High and low energy surfaces

Solid surfaces are divided in high-energy and low-energy surfaces. Solids with strong chemical bonds like metals, glasses and ceramics are strong and hard to break, which means that in order to break them, a big amount of energy is needed. Generally, liquids tend to have good affinity with these surfaces and perform total wetting. On the other hand, solid materials held together by weak forces like van der Waals forces are easy to break. This means that they are low energy surfaces and the degree of wetting will depend mostly on the type of fluid used [10, 11].

1.1.2 Capillary forces

Capillary forces are defined as interactions between contacting surfaces of solids and liquids, so the former are perturbed from their initial position and the latter from their initial shape. These perturbations cause collective self-assembly of particles at the macroscopic and even at the microscopic scales [8, 9].

Normal capillary-bridge forces

When two bodies are bridged by a drop phase, the capillary forces act normal to the contact line plane. Depending on the concavity of the bridging-drop, they can be attractive or repulsive, as illustrated in fig. 1.3. Attractive bridging forces are

responsible for the assembly of 3D structures of particles, i.e. a resistant sand castle on the beach is built by the assembly of water bridged sand-grains.
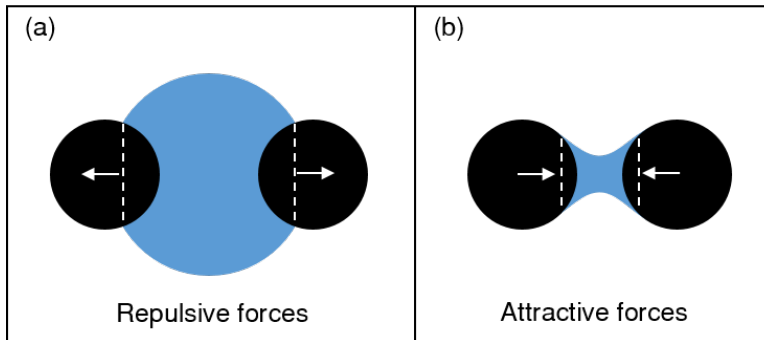
FIGURE 1.3 – (a) Convex bridging-drop generates repulsive capillary forces. (b) Concave bridging-drop generates attractive capillary forces.

Lateral capillary forces

If a body can cause a deflection on a free liquid interface, then two bodies put so close to each other that their deflections overlap forming menisci will induce lateral capillary forces. Depending on the menisci, the forces can be attractive (both are concave or both are convex) or repulsive (one is concave and the other is convex), as illustrated in fig 1.4. Attractive lateral forces are responsible for the structures in 2D, for instance paperclips self-assembling in the the fluid interface. It is worth highlighting that *capillary flotation forces* of particles are vertical immersion forces generated by the overlap of the interfacial deformations caused by two particles [12].
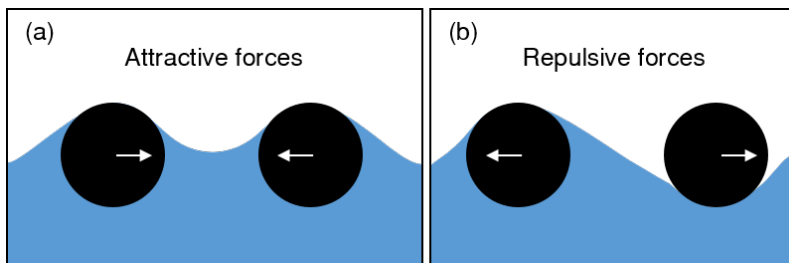
FIGURE 1.4 – (a) Two convex menisci generate attractive forces. (b) Concave and convex menisci generate repulsive forces.

1.2 Industrial applications

Binary-fluids and solid bodies interactions can be found in several important industrial processes. From many examples, a few are named below.

Stabilization of emulsion using particles
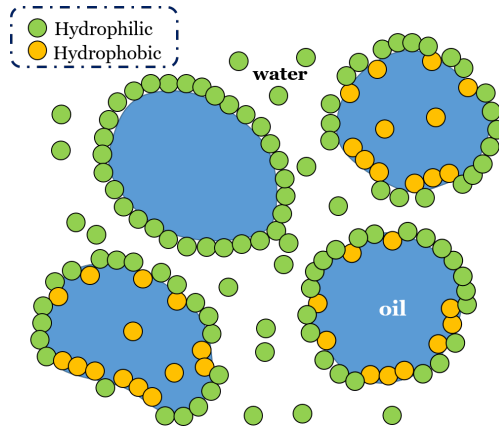
FIGURE 1.5 – Representation of emulsion stabilization with hydrophobic and hydrophilic particles.

An emulsion is usually defined as a mixture of two immiscible liquids [13], which remain in a form of small drops within the carrier fluid (usually oil drops in water) by adding emulsifiers like small particles (Pickering emulsions), whose wettable surface is hydrophilic, hydrophobic or both at the same time (Janus particles) [14]. The emulsion with particles then represent a ternary phase system. The applications of emulsions are countless, but they can be categorized into three groups: food (mayonnaise, butter, salad dressing, milk, etc.) [15], cosmetic (hair gels, moisturizers, etc.) [16] and pharmaceutical (creams and lotions) industries.
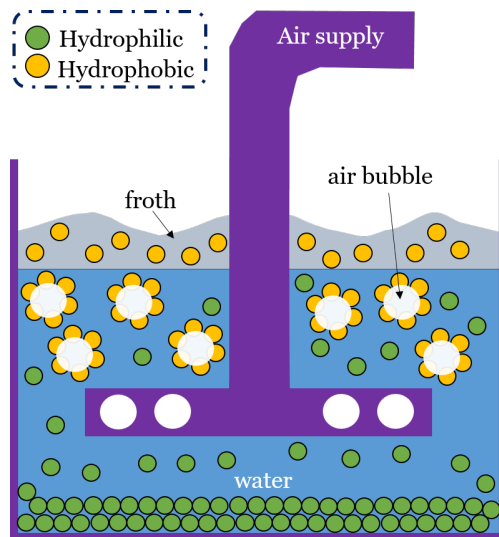
FIGURE 1.6 – Flotation froth process scheme.

Flotation froth process

One of the most common practices to separate hydrophobic and hydrophilic particles in a fluid is bringing one of them to the surface and collecting the other at the bottom of the tank. The flotation froth leverages on the hydrophobic nature of the particles which attach to the air-bubbles released at the bottom of the tank and are carried by them towards the surface (fig. 1.6).

Among the flotation techniques, only the froth flotation offers relevant industrial applications like mineral processing, paper recycling and wastewater treatment. Usually, the carrier fluid and particles are modified to increase the kinetic particle-bubble interaction in order to optimize the amount of desired particles in the froth [17].
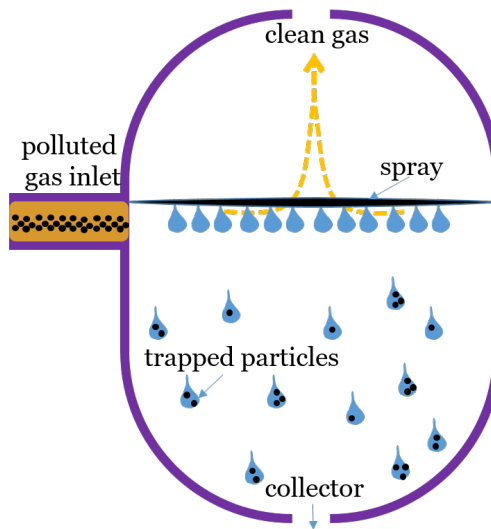
FIGURE 1.7 – Spray scrubbing process scheme.

Spray scrubbing process

Spray scrubbing process is used to filter harmful contaminants out of industrial exhaust gases before they are released to the environment [18]. The gas containing pollutant particles is canalized inside a chamber, where it is sprayed with scrubbing liquid. The drops trap the pollutant and drag it to the collector at the bottom of the chamber, leaving the exhaust gas clean to be released (fig. 1.7).

Apart from the above mentioned applications, we can mention the separation oil-coated spheres in aqueous solutions (oil and gas recovery), bubble absorption using hydrophobic springs, self-cleaning of superhydrophobic surfaces, inkjet printing [19], horizontal turbines working near water-air free surface (complex solid geometries interactions with two phase flows) [20], turbine cavitation particle erosion [21] and more. Some applications can be found in medicine, for instance a potential treatment procedure of artery thrombosis, as shown in fig. 1.8. The active compound (particles) is carried by drops driven by a laminar flow in the artery. Whenever the drops reach the

obstructed zone, the decrease in the channel diameter increases the shear rate, causing a deformation and a breakage of the drops, releasing the active compound into the zone to be treated [2].
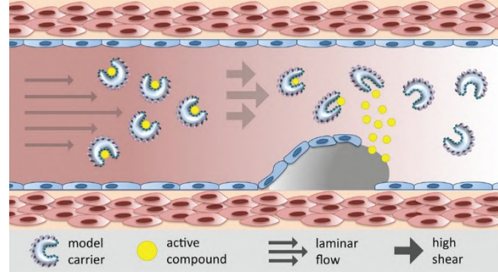
FIGURE 1.8 – High shear regime model for potential treatment of arterial thrombosis [2].

In the applications mentioned above, the solid-drop-liquid interactions represent a critical parameter which influences the overall performance of each process.

In literature, we can find numerous studies involving solid-solid interactions, which can be generally classified as collisions, drafting, kissing and tumbling, both experimentally [22] and numerically. While most of the simulations apply a sharp solid interface approach (such as for instance the Lattice-Boltzmann method [23, 24, 25, 26, 27] and the Immersed boundary method [28, 29, 30, 31, 32]), a smoothed particle interface of the solid has been recently gaining importance too, since the solid and the fluid phase are considered as a continuum [33, 34, 35, 36]. Extensive research has been done about interactions of two or more droplets and it is agreed that four types of collision may occur: bouncing, coalescence, separation and reflexive [37, 38, 39, 40, 41]. Although in recent years, there has been a growing interest in the research of interactions between solid and binary fluid interfaces, the repertory of solid-drop interaction studies in literature is still limited. A very interesting work on this topic was performed by Smith and Van de Ven in 1985 [42], who carried out experiments with a single sphere-droplet in a shear flow regime, using different capillary number (Ca) values, or experiments involving a pair of spheres and a droplet forming liquid bridged doublets. Another widely studied subject is a drop colliding into a sphere [43, 44, 45], as well as a small-spheres attachment to bubbles/droplets [46, 47, 48]. These kinds of interactions can be summarized as binary fluid with solid interactions, which not only refer to drops and particles in a carrier flow, but also to a sphere-free-surface interactions [49, 50, 51]. In the works mentioned above, the wettability effect is usually neglected. However, lately the studies have been increasingly interested in how wettability affects these ternary interactions, using hydrophobic, hydrophilic or neutral wettable solids fixed or moving in binary fluids (sphere-drop/bubble and sphere-free-surface) [52, 53, 54, 55].

Recently, the development of new approaches on how to numerically simulate ternary phase systems involving binary fluids and solid surfaces interactions has received a great deal of attention. Based on their complexity, the approaches that are currently available in literature can be grouped into 3 main categories. The first cat-

egory includes the approaches developed to treat flat wall boundaries. These are the ternary interactions simplest to implement, where the domain boundaries are treated as solid walls interacting with two distinct phases. The type of simulations allowed by this type of approach include, among others, channel flow laden with drops, bubbly flows in a tank and droplets impingement in flat surfaces [56, 57, 58, 59]. The second category includes the approaches developed to treat stationary arbitrary-shaped solid bodies. These approaches treat a static solid interface as a wall-boundary condition and are generally used to study problems such as porous media interactions with drops in a carrier fluid, drop impingement into curved surfaces, contact line evolution on a solid surface, meso-scale and macro-scale rigid structures immersed in a binary fluid [60, 61, 44, 62]. The third category includes the approaches developed to treat moving size-resolved solid particles in binary flows. In this case, the trajectory of the immersed particle can be altered by the fluid motion and by its own inertia. The studies carried out using this type of approaches are fully coupled and some of them present solid surface wetting effects. Therefore, their range of possible applications is vast, ranging from spheres sinking in water, buoyant bodies at water-air interface and sphere splashing into water to solid particles capture by drops and self-assembly induced by lateral capillary forces, just to name a few [26, 55, 53].

Although effective in simulating three phase interactions, the size-resolved methods usually need complex formulations and sophisticated numerical implementations. In this work, we present a simple and easy-to-implement numerical tool, where a Direct Numerical Simulation (DNS) of the incompressible carrier fluid flow is performed, the Phase Field Method describes the time evolution of the drop phase dynamics and the immersed solid particles are based on a hybrid Eulerian-Lagrangian description. These particles are tracked in a Lagrangian framework and their disturbance into the Eulerian domain of the fluid is spread using the Direct Forcing method. Their size and shape are bounded by a fictitious solid phase with a smooth interface. In addition, the wetting effects are also taken into account during ternary interactions. This allows to investigate two phenomena, neither of which have been previously numerically investigated to the best of the author's knowledge: the wetting effects in the submergence of a quasi-buoyant body and the relative rotation of two solids (bridged by a droplet), induced by shear fluid flow deformations on the drop interface.

Note

The present thesis includes the investigation results on multiphase fluids simulations carried out at the University of Udine, Italy during 21 months. The experimental results obtained during the 18 month secondment are reported in a published paper and technical inhouse reports to EHP.

1.3 Overview of the thesis

The thesis is organised as follows:

- Chap. 2: **Methodology** The governing equations controlling the temporal and

spatial evolution of the multiphase system are presented. First, different approaches used in literature to simulate binary fluids are introduced. The Phase Field Method is then described in detail, as it is the approach used in this thesis to track the interface. A solid fictitious phase immersed in a single-fluid is introduced afterwards, together with the motion and coupling equations under the Direct Forcing approach; the Phase Field Method is then modified, in order to develop a fully coupled ternary system. The fluid flow is obtained using a continuous approach. Finally, the numerical procedure employed in the discretization of the equation is presented.

- Chap. 3: **Solid phase immersed in a single fluid** In this chapter, our numerical implementation is validated, focusing on solids immersed in a carrier liquid, using analytical and experimental study cases as reference. The grid independence test is presented as well.

- Chap. 4: **Solid phase and binary fluid interface interactions results** The fully coupled ternary phase numerical algorithm is validated against experimental and analytical data available in literature. The wetting effects on the submergence of a quasi-buoyant disk are numerically investigated.

- Chap. 5: **Solid-drop pair interactions** In this chapter, the equilibrium configurations of a cylinder-drop pairs are studied at different contact angles and the results are compared with analytical solutions. In the second part, a Liquid Bridged Doublet is brought into the equilibrium configuration for an arbitrary contact angle. We follow with the study of the solids-drop interactions, when the LBD is placed within a shear flow field.

- Chap. 6: **Conclusions and future perspectives** A sum-up of the work done and results achieved during this PhD is presented, as well as the future research developments proposed by the author.

2

Methodology

In the first section (sec. 2.1) an overview of different approaches used to simulate multiphase flows is presented, with a special focus on the Phase field method, which is employed in this thesis. The method that describes the dynamics of a solid immersed in a single or binary fluid is described in sec. 2.2. Sec. 2.3 then introduces the flow field equations, the important dimensionless parameters and the dimensional analysis. Finally, sect. 2.4 describes the numerical method used to solve all the equations involved.

2.1 Binary systems simulation approaches

Over the last years, many approaches have been developed in order to simulate multiphase flows. Depending on how the interface si defined, these methods are classified in two categories: i) interface tracking and ii) interface capturing methods. The former represent the interface explicitly by using Lagrangian markers, while the latter rely on its implicit description, using a marker function, which is advected by the flow.

2.1.1 Front Tracking Method

The Front Tracking (FT) method is the most commonly used among the interface tracking methods [63, 64, 65]. A set of Lagrangian marker points are placed at the interface, they are advected by the local fluid and their position is calculated by the following equation:

$$\frac{\partial x^i}{\partial t} = \mathbf{u}^i, \tag{2.1}$$

where the position x^i is calculated by the interpolated local fluid velocity $\mathbf{u}^i$ for the $i - th$ marker. The interface is reconstructed after using a series of connections among the markers. The surface tension can be computed once the interface curvature is determined. The interfacial forces are then added to the Navier-Stokes equations by spreading their Lagrangian marker point value into the Eulerian grid (using a smoothing function). One of this method's disadvantages is the low accuracy of the curvature

computation and additional algorithms are needed to represent the topological changes in the interface, such as coalescence and breakage [66].

2.1.2 Volume of Fluid Method

The Volume of Fluid (VoF), is an interface capturing method, which solves an advection equation for an Eulerian marker function g:

$$\frac{\partial g}{\partial t} + \mathbf{u} \cdot \nabla g = 0. \tag{2.2}$$

The value of g_i is in every cell of a discretized domain calculated as the concentration volume average at each cell:

$$g_i = \frac{1}{V_i} \int_v g(x) dv, \tag{2.3}$$

g is initialized as a Heaviside step function. The evolution of g in eq. [2.2] leads to a numerical diffusion [66], which is why advection algorithms are used to reconstruct the shape of the interface [67, 68, 69]. The main advantages of this method are: i) coalescence and breakage are implicitly solved and ii) the mass is conserved in both phases.

2.1.3 Level Set Method

The Level Set (LS) method [70, 71] belongs to the group of interface capturing methods and it is an increasingly popular alternative to VoF. The interface is represented as the 0-level of a smooth function γ; the temporal evolution of γ is solved by the following advection equation:

$$\frac{\partial \phi}{\partial t} + \mathbf{u} \cdot \nabla f = 0. \tag{2.4}$$

The main idea is to define γ as the signed distance from the interface. The signed property is lost because of numerical diffusion and a reinitialization procedure is usually performed, ending up in a mass leakage between the phases. To fix this issue, the LS method is coupled with the VoF [72] and different marker functions profile are used [73]. In the same way as VoF, the Level Set method is accurate in the capture of coalescence and breakages, caused by the grid resolution instead of physical mechanisms.

2.1.4 Phase Field Method

The Phase Field Method (PFM) is an interface capturing method and it was initially developed to study the time-evolution of the alloy microstructure during a spinodal decomposition [74, 75, 76]. Later on, this method has been extended to the study of incompressible multiphase flows by introducing an advection term to the Cahn-Hilliard equation and a coupling term within the Navier-Stokes equations [77, 78]. In

this method, the Cahn-Hilliard equation (eq. [2.5]),

$$\frac{\partial \phi}{\partial t} + \mathbf{u} \cdot \nabla \phi = \nabla \cdot (\mathcal{M}_\phi \nabla \mu_\phi), \tag{2.5}$$

describes the evolution of the phase field order parameter (ϕ), which represents the local concentration of the phases and its value is constant at each phase but across the fluid-fluid interface thickness layer. The interface is advected by the velocity field ($\mathbf{u}$). The diffusive term, located on the right side of the equation, is constituted by the motility coefficient ($\mathcal{M}_\phi$) (relaxation time of the interface), which is set constant [79], and the chemical potential (μ_ϕ), derived as the variational derivative of a Ginzburg-Landau free-energy functional ($\mathcal{F}$) [78, 79]:

$$\mu_\phi = \frac{\delta \mathcal{F}[\phi, \nabla \phi]}{\delta \phi}. \tag{2.6}$$

For a system composed of two incompressible flows, the free-energy functional

$$\mathcal{F}[\phi, \nabla \phi] = \int_\Omega [f_b(\phi) + f_i(\nabla \phi)] \partial \Omega \tag{2.7}$$

has a contribution from the bulk (a double well potential, panel (a) in Fig. 2.1, with a minima for each pure phase)

$$f_b(\phi) = \frac{\alpha}{4}(\phi - \sqrt{\frac{\beta}{\alpha}})^2 (\phi + \sqrt{\frac{\beta}{\alpha}})^2, \tag{2.8}$$
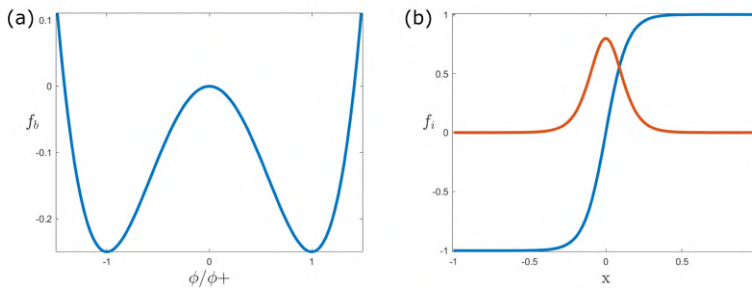
FIGURE 2.1 – (a) Double well potential. (b) Interface free-energy shown in red and the interface equilibrium profile plotted in blue.

    and the interface free energy density (which plays the role of surface tension for fluid-fluid interface, panel (b) in Fig. 2.1)

$$f_i(\nabla \phi) = \frac{\kappa}{2}|\nabla \phi|^2, \tag{2.9}$$

where κ is the value of the surface tension and α and β are the functional coefficients. From equation [2.6] to [2.9], the chemical potential results in the following expression:

$$\mu_\phi = \frac{\delta \mathcal{F}[\phi, \nabla\phi]}{\delta\phi} = \alpha\phi^3 - \beta\phi - \kappa\nabla^2\phi. \tag{2.10}$$

The phase field equilibrium occurs when the chemical potential is constant in the whole domain, $\nabla\mu_\phi = 0$, where the analytical solution and the equilibrium profile considering a flat interface is the following:

$$\phi = \phi_+ \tanh(\frac{\mathbf{s}}{\sqrt{2}\xi}), \tag{2.11}$$

where $\xi = \sqrt{\kappa/\beta}$ is the interfacial layer thickness, $\phi_+ = \sqrt{\beta/\alpha}$ indicates the value at each phase's bulk and $\mathbf{s}$ represents the interface normal coordinate.

The main advantages of the Phase Field method are i) the implicit description of topological changes like coalescence and breakage, ii) the accurate calculation of the interface curvature and shape, iii) the fact that advection schemes are not needed to maintain the interface profile in equilibrium. On the other hand, the PFM presents some drawbacks, for instance i) mass leakage (known also as shrinkage) induced by the combination of a chosen constant value for the mobility and double-well potential [80, 81], ii) coarsening phenomena resulting from the energy minimization criterion (in domains with one large phase and a small one, the former tends to grow over the latter in order to reduce the domain interfacial energy) and iii) overshots and undershots in the phase field over the entire domain, which lead to nonphysical values of the surface tension, as well as to negative values in density and viscosity.

2.2   Solid-phase and binary fluid coupling

In this work the solid body trajectories are treated as point-wise particles in a Lagrangian framework. Each particle position is mapped in the Eulerian domain and linked to a region with a resolved shape and size of the corresponding solid body. Similar to You et al. [82] a Direct Forcing method is applied in this region, however, we describe the solid interface as a transition layer from the solid region to the fluid bulk using a smooth function in order to ensure the compatibility with the PFM [83, 36].

2.2.1   Single fluid and rigid-solid interaction approach

A generic incompressible Newtonian fluid flow is introduced as the carrier fluid flow, governed by the Navier-Stokes and continuity equations:

$$\nabla \cdot \mathbf{u} = 0, \tag{2.12}$$

$$\rho \left[\frac{\partial \mathbf{u}}{\partial t} + (\mathbf{u} \cdot \nabla)\mathbf{u} \right] = -\nabla P + \mu\nabla^2\mathbf{u} + \rho\mathbf{g}. \tag{2.13}$$

Considering that the solid phase is described by a fictitious domain (Ω_s) built up

by the union of n individual body fields:

$$\Omega_s = \bigcup_{i=1}^{n} \Omega_i, \tag{2.14}$$

a phase parameter ψ_s is inserted with constant values in the solid and fluid bulk volume ($\psi_s = 1$ and $\psi_s = 0$, respectively). The transition between phases is represented by a smooth layer, where fluid and solid properties coexist in proportions ruled by a hyperbolic tangential profile along the normal direction of the solid interface $\mathbf{x}$. In order to properly describe the local properties, the grid resolution must ensure the thinnest width with a well defined transition profile. Every individual rigid-solid sphere can then be generated using the following expression:

$$h(\mathbf{x}) = \frac{1}{2}[1 - tanh(\frac{\mathbf{x} - \mathbf{r}}{\xi_s})], \tag{2.15}$$

which is similar to the formulation used by Nakayama et al. [84], where $\mathbf{r}$ is the solid radius and ξ_s is the parameter control for the interface width.

The fluid-solid coupling is achieved by adding a virtual force into the Navier-Stokes equations following the Direct Forcing Immersed Boundary approach [85, 86, 87]. In this method, the fluid within the solid region is enforced to follow prescribed solid-bodies velocities, ensuring the rigidity and the non-penetration condition [82].

The modified Navier-Stokes equations are:

$$\rho \left[\frac{\partial \mathbf{u}}{\partial t} + (\mathbf{u} \cdot \nabla)\, \mathbf{u} \right] = -\nabla P + \mu \nabla^2 \mathbf{u} + \rho \mathbf{g} + \rho \boldsymbol{f}_{DF}. \tag{2.16}$$

where $\boldsymbol{f}_{DF}$ is the virtual force exerted in the solid region Ω_s to advance the solid object velocity from an intermediate time level velocity field $\mathbf{u}^*$ (where no influence of the solid is considered for its resolution) to $\mathbf{u}_s^{n+1}$ (calculated in previous steps) [82, 36, 88]. Eq. [2.17] shows how $\boldsymbol{f}_{DF}$ is calculated.

$$\boldsymbol{f}_{DF} = \frac{\mathbf{u}_s^{n+1} - \mathbf{u}^*}{\Delta t}, \tag{2.17}$$

where Δt is the integration time step.

2.2.2 Equations of motion for a solid immersed in a fluid

The solid phase dynamics is described in a Lagrangian frame. The motion of an immersed rigid-body is caused by lineal and angular momentum. Consequently, the velocity $\mathbf{u}_s$ of the rigid-body can be decomposed in a translational and rotational velocity, as shown in eq. [2.18]:

$$\mathbf{u}_s = \mathbf{v}_s + \omega_s \times \mathbf{r}, \tag{2.18}$$

where $\mathbf{v}_s$ is the immersed-solid linear velocity and ω_s its angular velocity with respect to the axis passing through its center of mass.

(i) We use the equation derived by Cheng-Shu et al. [82], shown in eq. [2.19], in order to obtain the lineal velocity of the solid object.

$$m_s \frac{d\mathbf{v}_s}{dt} = (m_s - m_f)g - \iiint\limits_{\Omega} \psi_s \rho_f f dV + m_f \frac{d\mathbf{v}_s}{dt}, \qquad (2.19)$$

where m_s and m_f are the solid and the fluid mass respectively, g represents the gravity and f is the average value of virtual force for the solid. The terms in the RHS of eq. [2.19] accounts on the effects of buoyancy, inertia and added mass (read from left to right). Subsequently this equation is discretized in time considering the following equivalences:

$$m_s = \iiint\limits_{\Omega_s} \rho_s f dV = \iiint\limits_{\Omega} \psi_s \rho_s f dV \qquad (2.20)$$

and

$$m_f = \iiint\limits_{\Omega_s} \rho_f f dV = \iiint\limits_{\Omega} \psi_s \rho_f f dV \qquad (2.21)$$

and for the virtual force term we use a 2$^{\text{nd}}$-order-accurate Adams-Bashforth scheme, obtaining as a result the following expression :

$$m_s \frac{\mathbf{v}_s^{n+1} - \mathbf{v}_s^n}{\Delta t} = (m_s - m_f)g - (\frac{3}{2} \iiint\limits_{\Omega_s} \rho_f f^n dV - \frac{1}{2} \iiint\limits_{\Omega_s} \rho_f f^{n-1} dV) + m_f \frac{\mathbf{v}_s^n - \mathbf{v}_s^{n-1}}{\Delta t}.$$
$$(2.22)$$

(ii) The angular momentum can be calculated from the intermediate time level velocity field $\mathbf{u}^*$ as follows:

$$\mathbf{J}_s \omega_s = \iiint\limits_{\Omega_s} \rho_s \mathbf{r} \times \mathbf{u}^*, \qquad (2.23)$$

where $\mathbf{J}_s$ is the rotational inertia of the solid body, $\mathbf{r} = \mathbf{x} - \mathbf{X}_s$ is the relative vector of a spatial point ($\mathbf{x}$) to the the center of mass of the solid body ($\mathbf{X}_s$). From eq. [2.23], we can calculate the angular rotation of the body center-of-mass.

Finally, the body trajectory is calculated by integrating the following expression:

$$\frac{d\mathbf{X}_s}{dt} = \mathbf{u}_s. \qquad (2.24)$$

2.2.3   Particle collisions

Collisions between particles and wall and particle and particle are very important in particle-laden flows, especially in situations where the solid phase concentration is dense, for systems with high Reynolds number or higher probability of collisions due to a specific mechanism, such as two solids at a binary fluid interface brought together by the action of capillary forces.

Generally, the grids used for DNS are not fine enough to solve lubrication in the gap between a particle in close proximity to another particle or a solid boundary, which creates the need for numerical schemes to account for the collision.

Glowinski et al. [33] introduced a simple method which consists of a short range repulsive force acting in the particle when the gap between the particle and the other entity is lower than a given threshold (safe zone) set in advance. The repulsive force between a particle and a solid boundary is given by the reflection method. Later on, Feng and Michaelides [89] improved this technique, with the aim to avoid particles overlapping (hard collision) without having undesired side effects, by using a two step function for soft and hard collision. The collision of two spherical particles is given by the following scheme:
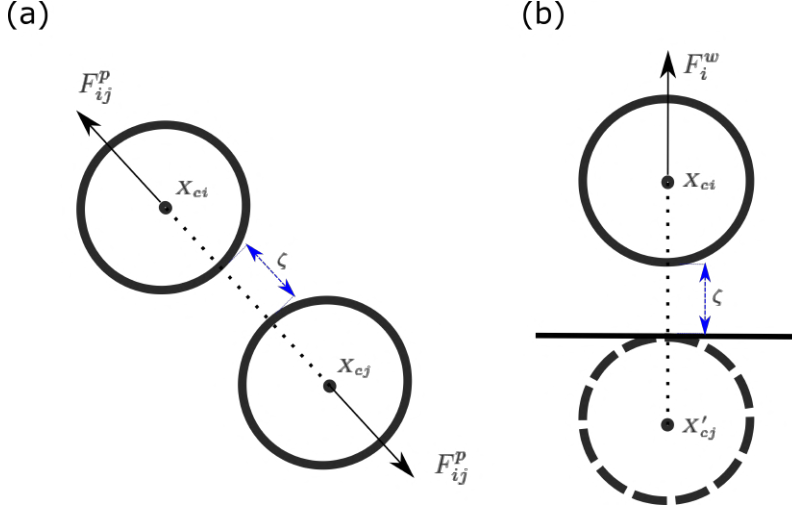
FIGURE 2.2 – (a) particle-particle collision (b) reflection method for particle-wall collision.

$$
F_{ij}^p = \begin{cases}
0, & ||\mathbf{X}_{ci} - \mathbf{X}_{cj}|| \geq D_p + \zeta \\
\frac{c_{ij}}{\epsilon_{pp}} \mathcal{B}_{pp}(\frac{\mathbf{X}_{ci} - \mathbf{X}_{cj}}{||\mathbf{X}_{ci} - \mathbf{X}_{cj}||}), & D_p \leq ||\mathbf{X}_{ci} - \mathbf{X}_{cj}|| < D_p + \zeta \\
\frac{c_{ij}}{\epsilon_{pp}}(\mathcal{B}_{pp} + \frac{c_{ij}}{E_{pp}}(\frac{D_p - ||\mathbf{X}_{ci} - \mathbf{X}_{cj}||}{\zeta}))(\frac{\mathbf{X}_{ci} - \mathbf{X}_{cj}}{||\mathbf{X}_{ci} - \mathbf{X}_{cj}||}), & ||\mathbf{X}_{ci} - \mathbf{X}_{cj}|| \leq D_p
\end{cases}
$$

with:

$$
\mathcal{B}_{pp} = \left(\frac{||\mathbf{X}_{ci} - \mathbf{X}_{cj}|| - D_p - \zeta}{\zeta} \right)^2,
$$

and for the collision of a sphere with a wall,

$$
F_i^w = \begin{cases}
0, & ||\mathbf{X}_{ci} - \mathbf{X}'_{ci}|| \geq D_p + \zeta \\
\frac{c_{ij}}{\epsilon_{pw}} \mathcal{B}_{pw}(\frac{\mathbf{X}_{ci} - \mathbf{X}'_{ci}}{||\mathbf{X}_{ci} - \mathbf{X}'_{ci}||}), & D_p \leq ||\mathbf{X}_{ci} - \mathbf{X}'_{ci}|| < D_p + \zeta \\
\frac{c_{ij}}{\epsilon_{pw}}(\mathcal{B}_{pw} + \frac{c_{ij}}{E_{pw}}(\frac{D_p - ||\mathbf{X}_{ci} - \mathbf{X}'_{ci}||}{\zeta}))(\frac{\mathbf{X}_{ci} - \mathbf{X}'_{ci}}{||\mathbf{X}_{ci} - \mathbf{X}'_{ci}||}), & ||\mathbf{X}_{ci} - \mathbf{X}'_{ci}|| \leq D_p
\end{cases}
$$

with:

$$\mathcal{B}_{pw} = \left(\frac{||\mathbf{X}_{ci} - \mathbf{X}'_{cj}|| - D_p - \zeta}{\zeta} \right)^2,$$

where $\mathbf{X}_{ci}$ is the center coordinate of the i-th sphere and $\mathbf{X}'_{ci}$ is the center coordinate of the imaginary particle reflected, attached to the other side of the wall (see fig. 2.2), c_{ij} is chosen as a constant force scaled (usually the buoyancy force is used) [31], ϵ_{pp} and ϵ_{pw} are the stiffness parameters for the collision, E_{pw} and E_{pp} are smaller parameters (bigger spring force) than ϵ, in order to ensure non-overlapping particles. We choose the values of $\epsilon_{pp} = 0.25$, $\epsilon_{pw} = 0.5$ and $E_{pp} = E_{pw} = 0.02$, following Feng et al. [89]. The parameter ζ is the chosen threshold to activate the collision scheme.

Fig. 2.3 shows the time sequence of the collision between two approaching spheres driven by a shear flow in a closed channel. Panel (a) shows the two objects approaching and how they are arranged to ensure the interaction. Panel (b) shows the moment when the disks reach contact and in panel (c) they briefly bounce back (caused by the normal reaction force of the collision). Shortly after, the motion of the spheres is taken over by the stream force. Since the kinetic energy is lower after the first collision, the bodies attach smoothly at the contact point and start rotating and sliding as a coupled system (panel (d)). Finally, when the normal-collision-force becomes zero (panel (e)), the two disks slide away, break the contact and follow freely the fluid stream again.
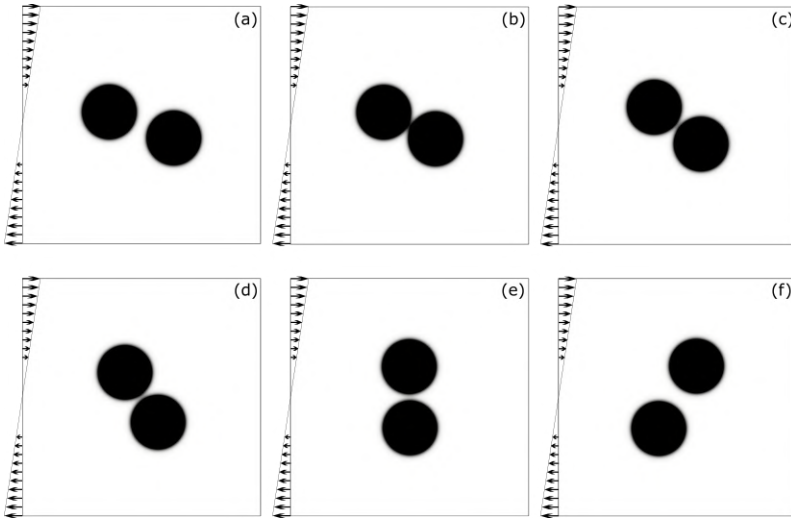
FIGURE 2.3 – Collision time sequence of 2 disks: (a) approaching disks, (b) collision (c) back-bouncing, (d) rolling around contact point, e) tangential sliding and (f) separation.

2.2.4   Fictitious solid-phase with wettability in immiscible binary fluids

In order to include the wettability effects of a solids immersed in a binary fluid model, we modify the free energy density functional (eq. [2.7]), following the approach pre-

sented by Shinto [55]. This is based on the model of Cahn [90], who adds an additional surface term $\mathcal{F}_s$ (eq. [2.25]) to describe the interactions between a binary fluid interface and a solid.

$$\mathcal{F}_s[\mathbf{X}_s, t] = \frac{1}{\beta} \int_S (-H\psi_s) dS, \qquad (2.25)$$

where $\mathbf{X}_s$ is the position of the particle and S is the particle surface. H is pre-assigned parameter to control the wettability and it admits values within the range of $\phi_f = -1$ and $\phi_d = +1$ (these range limits correspond to the values of the order parameter ϕ at the bulk of each phase in the binary system). For a value of $H = 0$, the solid surface is neutrally wettable, in the case of $H < 0$, the solid has more affinity to the fluid and when $H > 0$, the solid surface experiences more attraction to the drop. ψ_s is the compositional order parameter of the solid. The binary fluid should evolve nearby this region, in order to accomplish the minimization of the free energy of the system [55, 61]. The equilibrium contact angle (θ_{eq}) with respect to the affinity value can be calculated with the following expression:

$$cos(\theta_{eq}) = \frac{\mathcal{X}_S}{2}(3 - \mathcal{X}_S^2), \qquad (2.26)$$

with

$$\mathcal{X}_S = \frac{\psi_p - \bar{\phi}_S}{\phi_d - \bar{\phi}_S} \qquad (2.27)$$

and

$$\bar{\phi}_S = \frac{\phi_f + \phi_d}{2}, \qquad (2.28)$$

where $\bar{\phi}_S$ and $\mathcal{X}_S$ describe the homogeneous solid surface and its affinity ($-1 \le \mathcal{X}_S \le 1$) [61]. A similar approach of implicitly imposing the contact angle by using an affinity parameter was developed by Guillaument et al. [57], who impose wetting effects using the penalty method.

The modified free energy functional considering the solid phase ψ_s and the fluid phase $(1 - \psi_s)$ is shown in eq. [2.29]:

$$\mathcal{F}[\phi, \psi_s] = \frac{1}{\beta} \int_V d\mathbf{x}[f_b(\phi) + \frac{\kappa}{2}|\nabla\phi|^2 + \frac{K_s}{2}(\phi - \psi_p)^2 \psi_s], \qquad (2.29)$$

where ψ_p is a constant value controlling the affinity, K_s is a positive parameter (which has to be chosen as a large value compared with the parameters α and β) which ensures the value of the affinity inside the solid region in the phase field by imposing a single-well potential in the free energy functional [55].

The additional solid coupling term in the free energy functional makes the chemical potential (eq. [2.10]) evolve into the following expression:

$$\mu_\phi = \frac{\delta\mathcal{F}[\phi, \psi_s]}{\phi} = \alpha\phi^3 - \beta\phi - \kappa\nabla^2\phi + K_s(\phi - \psi_p)\psi_s. \qquad (2.30)$$

In order to ensure the no-penetration condition, we employ the operator $(\mathbf{I} - \mathbf{n_s} \otimes \mathbf{n_s})$, which acts directly in the solid diffused interface, with $\mathbf{n_s} = \nabla\psi_s/|\nabla\psi_s|$ as the

solid surface normal vector and $\mathbf{I}$ as the unit tensor. The advection-diffusion equation, taking into account the solid phase, results as follows:

$$\frac{\partial \phi}{\partial t} + \mathbf{u} \cdot \nabla \phi = \mathcal{M}_\phi \nabla \cdot [(\mathbf{I} - \mathbf{n_s} \otimes \mathbf{n_s})(\nabla \mu_\phi)]. \tag{2.31}$$

2.3   Flow Field Equations

The equations that fully describe the incompressible flow of a generic Newtonian fluid with advected and deformable interfaces are the continuity equation (mass conservation) and the Navier-Stokes equations (momentum conservation) with an interfacial term (representing the coupling with the Cahn-Hilliard equation) and a virtual force term to account for the feedback of rigid-immersed bodies. The dimensional form of the mass conservation equation for incompressible flows is as follows:

$$\nabla \cdot \mathbf{u} = 0. \tag{2.32}$$

In order to couple the two-phases-flow-field, we use a continuous approach to introduce boundary conditions at the interface [91, 92]. As for velocity, the transition at the interface should be continuous, avoiding sudden jumps, as shown in the following expression:

$$\mathbf{u}_1 \cdot \mathbf{n} - \mathbf{u}_2 \cdot \mathbf{n} = 0, \tag{2.33}$$

where $\mathbf{n}$ is the unit normal tensor to the interface and $\mathbf{u}_1$ and $\mathbf{u}_2$ represent the velocity vectors at each side of the interface. The jump condition for the stress tensor at the interface can be written as follows:

$$\mathbf{T}_1 \cdot \mathbf{n} - \mathbf{T}_2 \cdot \mathbf{n} = \mathcal{K}\sigma\mathbf{n} - \nabla_s \sigma, \tag{2.34}$$

where $\mathcal{K}$ is the mean curvature, σ is the surface tension, and $\mathbf{T}_1$ and $\mathbf{T}_2$ are the stress tensors at each side of the interface. The rhs of eq. [2.34] is composed by a normal ($\mathcal{K}\sigma\mathbf{n}$) and a tangential ($\nabla_s \sigma$) component, with ∇_s being the surface gradient operator.

The Navier-Stokes equations using the continuous approach in the binary fluid for a divergence-free velocity field are:

$$\begin{aligned} \rho\left(\phi\right)\left[\frac{\partial \mathbf{u}}{\partial t} + \left(\mathbf{u} \cdot \nabla\right)\mathbf{u}\right] = &-\nabla P + \nabla \cdot \left[\eta\left(\phi\right)\left(\nabla\mathbf{u} + \nabla\mathbf{u}^T\right)\right] + \rho\left(\phi\right)\mathbf{g} \\ &+ \nabla \cdot \left[\bar{\tau}_c \mathcal{K}\sigma\right] + \rho\left(\phi\right)\boldsymbol{f}_{DF}\left(\psi_s\right), \end{aligned} \tag{2.35}$$

with $\mathbf{u} = (u, v, w)$ as the velocity field, $\rho\left(\phi\right)$ and $\eta\left(\phi\right)$ as the local density and dynamic viscosity respectively, $\bar{\tau}_c$ as the Korteweg tensor, σ as the surface tension and $\boldsymbol{f}_{DF}$ as the virtual force exerted by the solid phase.

2.3.1 Non-matched properties treatment

In order to avoid numerical discontinuities and jumps across the interface, the thermo-physical properties are defined to depend on the phase field indicator ϕ with smooth transitions across the interface.
We select arbitrarily the carrier phase ($\phi = -\sqrt{\beta/\alpha}$) as the reference property value, then the local density and viscosity are defined as:

$$\rho(\phi) = \rho_c \left[1 + \frac{\rho_r - 1}{2} (\frac{\phi}{\sqrt{\beta/\alpha}} + 1) \right], \tag{2.36}$$

$$\eta(\phi) = \eta_c \left[1 + \frac{\eta_r - 1}{2} (\frac{\phi}{\sqrt{\beta/\alpha}} + 1) \right], \tag{2.37}$$

with:

$$\rho_r = \frac{\rho_d}{\rho_c}, \quad \eta_r = \frac{\eta_d}{\eta_c}, \tag{2.38}$$

where the subscript d indicates the dispersed phase and c the carrier phase.
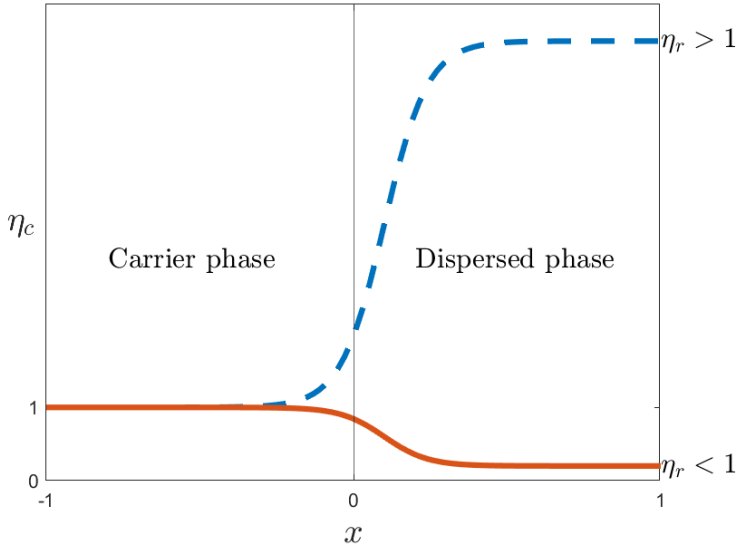
FIGURE 2.4 – Transition profile of the dynamic viscosity when η_r is greater than 1 (dashed-blue curve) and when η_r is smaller than 1 (red-plain curve). The interface is identified by the vertical gray line.

We display two different dynamic viscosity ratios in fig. 2.4 ($\eta_r < 1$ and $\eta_r > 1$), which shows that the definition of the equations [2.36] and [2.37] prevents the value to reduce below zero (unphysical values).

2.3.2   Non-dimensional Formulation

The scheme of the three-dimensional domain that we use for our simulations is shown in fig. 2.5, where the upper and lower boundaries consist in infinite parallel walls separated $L_z = 2h$ from each other.
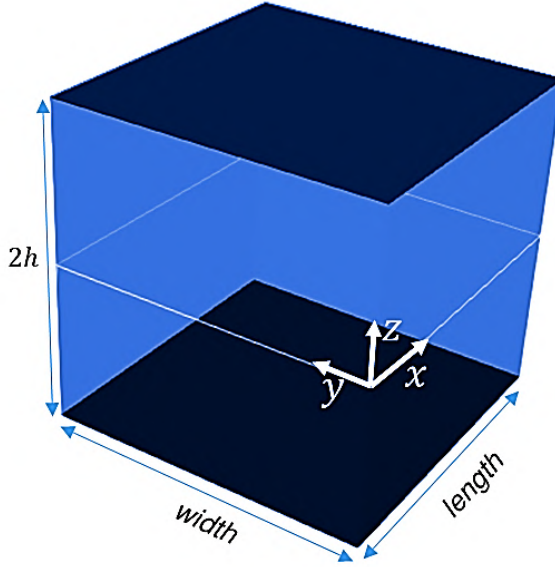
FIGURE 2.5 – Scheme of the three dimensional domain with the upper and lower boundary as walls and with periodic conditions in x and y directions.

All the equations are solved in a non-dimensional form. The Navier-Stokes equation is turned into non-dimensional by introducing the so-called outer-scaling units (indicated by the "*" apex). On that account we define the characteristic flow scales: as a characteristic length scale we use the semi-height h of periodic side of the domain and for the velocity we use the classical definition of shear velocity u_τ:

$$u_\tau = \sqrt{\frac{\tau_w}{\rho_c}}, \tag{2.39}$$

where τ_w is the mean value of the shear at the wall.

All the variables of our interest can now be transformed in a non-dimensional form as follows:

$$\mathbf{x}^* = \frac{\mathbf{x}}{h}, \qquad \mathbf{u}^* = \frac{\mathbf{u}}{u_\tau}, \qquad t^* = \frac{t u_\tau}{h}, \qquad P^* = \frac{P}{\rho u_\tau^2} \tag{2.40}$$

with $\mathbf{x} = (x, y, z)$ as position, $\mathbf{v} = (u, v, w)$ as velocity, t as time and P as pressure. It is thus possible to obtain (with some simple substitutions) the following expressions for the continuity and Navier-Stokes equations:

$$\nabla \mathbf{u}^* = 0, \tag{2.41}$$

$$\rho^* (\phi^*) \left[\frac{\partial \mathbf{u}^*}{\partial t^*} + (\mathbf{u}^* \cdot \nabla) \mathbf{u}^* \right] = -\nabla P^* + \frac{1}{Re_\tau} \nabla \cdot \left[\eta^* (\phi^*) \left(\nabla \mathbf{u}^* + \nabla \mathbf{u}^{*T} \right) \right] +$$
$$\frac{1}{Fr^2} \rho^* (\phi^*) \mathbf{g}^* + \frac{3Ch}{\sqrt{8}We} \nabla \cdot [\bar{\tau}_c^* \mathcal{K}] + \tag{2.42}$$
$$\rho^* (\phi^*) \boldsymbol{f}_{DF}^* (\psi_s^*),$$

where $\mathbf{g}^*$ is the gravity unit vector, the shear Reynolds number Re_τ is defined as:

$$Re_\tau = \frac{\rho_c \mathbf{u}_\tau h}{\eta_c} = \frac{\mathbf{u}_\tau h}{\nu}, \tag{2.43}$$

with $\nu[\frac{m}{s^2}]$ as kinematic viscosity; the Weber number is defined as:

$$We = \frac{\rho_c \mathbf{u}_\tau^2 h}{\sigma}, \tag{2.44}$$

where σ is the surface tension. The Froude number is then defined as:

$$Fr = \frac{u_\tau}{\sqrt{gh}}; \tag{2.45}$$

the Cahn number represents the ratio between the characteristic length scales of the interface and the fluid domain:

$$Ch = \frac{\xi}{h}. \tag{2.46}$$

The non-dimensional form of the transport equation for the phase field becomes:

$$\frac{\partial \phi^*}{\partial t^*} + \mathbf{u}^* \cdot \nabla \phi^* = \frac{1}{Pe_\phi} \nabla^2 \mu_\phi^*, \tag{2.47}$$

where the phase field Péclet number $(Pe_\phi = u_\tau h / (\beta \mathcal{M}_\phi))$ measures the ratio between convection and diffusion in the phases, were $\mathcal{M}_\phi$ is the constant mobility coefficient for the phase field. The non-dimensional form of the phase field equilibrium profile is:

$$\phi^* = \frac{\mathbf{s}^*}{\sqrt{2}Ch}, \tag{2.48}$$

with $\mathbf{s}^*$ as a non-dimensional coordinate normal to the interface. Using the factor $\frac{\beta^3}{\alpha}$, the chemical potential becomes non-dimensional:

$$\mu_\phi^* = \phi^{*3} - \phi^* - Ch^2 \nabla^2 \phi^* + (\phi^* - \psi_p)\psi_s. \tag{2.49}$$

The phenomenological behavior of the analyzed problem is set by the shear Reynolds

number and the Weber number. The Cahn number represents the ratio between the binary fluid interface thickness and the domain height, therefore, its value is set according to the computational mesh grid. The Cahn number is usually chosen to have at least five grid points across the interface. The phase field Péclet number (Pe_ϕ), is then set taking into account the Cahn number: $Pe\phi = 1/Ch$ [93, 94].

The non-dimensional equations for the solid body are found using the characteristic parameters employed in the phase field equations, eq. [2.19] becomes:

$$\frac{d\mathbf{v}_s^*}{dt^*} = \frac{1}{Fr^2}\left(1 - \frac{\rho_{fsub}}{\rho_s}\right)\mathbf{g}^* - \frac{\rho_{fsub}}{\rho_s}\left(f + \frac{d\mathbf{v}_s^*}{dt^*}\right), \tag{2.50}$$

where ρ_s is the solid body density and ρ_{fsub} is the average value of the fluid density in the region occupied by the solid. The latter can be calculated in the following way: $\rho_{fsub} = \rho_A(I_{ss}) + \rho_A(1 - I_{ss})$, where I_{ss} is the immersed volume portion with respect to the fluid A described in appendix A.1, ρ_A and ρ_B are the densities of fluid A and B respectively.

2.4 Numerical method

In order to solve the flow field we use the velocity-vorticity approach, where the momentum and the continuity equations are exchanged by the second-order equation for the wall-normal component of the vorticity (curl of the Navier-Stokes equations), the fourth-order equation for the wall-normal component of the velocity (twice the curl of the Navier-Stokes equations), the equation of the wall-normal vorticity and the continuity equation. With this approach, we avoid solving the pressure field and the use of time consuming Poison solvers.

2.4.1 Velocity-vorticity Formulation

For the numerical resolution of the flow equations, it is very useful to rewrite the continuity and Navier-Stokes equations without taking explicitly into account the pressure $\frac{\partial p}{\partial x}$ gradient term by taking the curl of the non-dimensional momentum equation (eq. [2.42]) rearranged by collecting the non-linear terms into **S** and by removing the superscripts for briefness:

$$\frac{\partial \mathbf{u}}{\partial t} = \mathbf{S} + \frac{1}{Re_\tau}\nabla^2\mathbf{u} - \nabla P', \tag{2.51}$$

with

$$\mathbf{S} = -\mathbf{u}\cdot\nabla\mathbf{u} - \frac{\rho_r - 1}{2}\left(1 + \phi\right)\left(\frac{\partial\mathbf{u}}{\partial t} + \mathbf{u}\cdot\nabla\mathbf{u}\right) - \Pi + \rho(\phi)\boldsymbol{f}_{DF}(\psi_s)$$

$$+ \frac{1}{Re_\tau}\nabla\cdot\left[\frac{\eta_r - 1}{2}\left(1 + \phi\right)\left(\nabla\mathbf{u} + \nabla\mathbf{u}^T\right)\right] + \frac{\rho(\phi)\mathbf{g}}{Fr^2} + \frac{3Ch}{\sqrt{8}We}\nabla\cdot\bar{\tau}_c,$$

where the pressure gradient is split into two: a mean, Π and a fluctuating pressure gradient, $\nabla P'$. Then taking the curl:

$$\nabla \times \frac{\partial \mathbf{u}}{\partial t} = \nabla \times \mathbf{S} + \frac{1}{Re_\tau} \nabla \times \nabla^2 \mathbf{u} - \nabla \times \nabla P^{'}. \tag{2.52}$$

If we now observe that the last term is precisely zero (because of a vectorial identity) and if we recall the definition of the vorticity vector $\boldsymbol{\omega} = \nabla \times \mathbf{u}$, it follows:

$$\frac{\partial \boldsymbol{\omega}}{\partial t} = \nabla \times \mathbf{S} + \frac{1}{Re_\tau} \nabla^2 \boldsymbol{\omega}, \tag{2.53}$$

which is an alternative expression of the vorticity transport equation. If we now take again the curl of this equation and we use the identity $\nabla \times \nabla \times \mathbf{c} = \nabla (\nabla \cdot \mathbf{c}) - \nabla^2 \mathbf{c}$ (which applies to every vectorial field $\mathbf{c}$) and the continuity equation, the result will be the following Helmoltz fourth order equation:

$$\frac{\partial (\nabla^2 \mathbf{u})}{\partial t} = \nabla^2 \mathbf{S} - \nabla (\nabla \cdot \mathbf{S}) + \frac{1}{Re_\tau} . \nabla^4 \mathbf{u}. \tag{2.54}$$

The classic resolution algorithm velocity-normal vorticity developed by [95] requires projecting the eq. [2.53] and [2.54] in the wall normal direction and solving them, in order to obtain the wall normal components w and ω_z. The continuity equation and the definition of vorticity are then used to calculate the other two velocity components (u and v).
The system employed for the numerical resolution of a fluid flow in our domain is thus described by:

$$\frac{\partial \omega_z}{\partial t} = \frac{\partial S_y}{\partial x} - \frac{\partial S_x}{\partial y} + \frac{1}{Re_\tau} \nabla^2 \omega_z, \tag{2.55}$$

$$\frac{\partial (\nabla^2 w)}{\partial t} = \nabla^2 S_z - \frac{\partial}{\partial z} \left(\frac{\partial S_x}{\partial x} + \frac{\partial S_y}{\partial y} + \frac{\partial S_z}{\partial z} \right) + \frac{1}{Re_\tau} \nabla^4 w, \tag{2.56}$$

$$\frac{\partial u}{\partial x} + \frac{\partial v}{\partial y} = -\frac{\partial w}{\partial z}, \tag{2.57}$$

$$\frac{\partial v}{\partial x} + \frac{\partial u}{\partial y} = \frac{\partial \omega_z}{\partial z}. \tag{2.58}$$

Once the velocity field is calculated, the fluctuating component of the pressure can be obtained by the following Poisson-like equation:

$$\nabla^2 P^{'} = \nabla \cdot \mathbf{S}. \tag{2.59}$$

2.4.2   Cahn-Hilliard equation stability splitting term

The Cahn-Hilliard equation solution involves high order operators which require robust numerical schemes. By introducing eq. [2.49] into eq. [2.47], the 4th order operator is evident:

$$\frac{\partial \phi}{\partial t} = -\mathbf{u} \cdot \nabla \phi + \frac{1}{Pe_\phi} \left(\nabla^2 \phi^3 - \nabla^2 \phi - Ch^2 \nabla^4 \phi + \nabla^2 \left[(\phi - \psi_p) \psi_s \right] \right). \tag{2.60}$$

To improve the stability, we adopt the same pseudo-spectral scheme used for solving the Navier-Stokes equation, rearranging eq. [2.60] we obtain:

$$\frac{\partial \phi}{\partial t} = S_\phi + \frac{sCh^2}{Pe_\phi}\nabla^2 \phi - \frac{Ch^2}{Pe_\phi}\nabla^4 \phi, \qquad (2.61)$$

where we use the operator splitting $\nabla^2 \phi = (sCh^2 + 1)\nabla^2 \phi - sCh^2\nabla^2 \phi$ similar to the one presented in [96], where a positive coefficient s is selected based on the temporal discretisation, using in our case $s = \sqrt{4Pe_\phi Ch^2/\Delta t}$ [79, 97]. Then we collect the convective term, the non-linear term, the solid phase term and the term produced after the splitting process into S_ϕ:

$$S_\phi = -\mathbf{u} \cdot \nabla \phi + \frac{1}{Pe_\phi}\nabla^2 \phi^3 - \frac{(sCh^2 + 1)}{Pe_\phi}\nabla^2 \phi + \nabla^2\left[(\phi - \psi_p)\psi_s\right]. \qquad (2.62)$$

2.4.3   Spectral Space discretization

We use the pseudo-spectral spatial discretization to solve equations 2.55, 2.56 and 2.60, where the solutions are approximated via Fourier transforms along the two periodic directions of our domain (direction x and y in fig. 2.5) and the Chebyshev polynomials are used for the solution approximation in the wall-normal direction. All multiplications in the Fourier-Chebyshev space are avoided by transforming spectral variables back into the physical space where the multiplication is performed, and then re-transformed into the spectral space. Due to this process, the algorithm is called "pseudo-spectral".

The following sum of harmonics represents the projection of a signal g along the periodic directions x and y into the Fourier space:

$$g(x, y, z) = \sum_{n_x = -\frac{N_x}{2}+1}^{\frac{N_x}{2}} \sum_{n_y = -\frac{N_y}{2}+1}^{\frac{N_y}{2}} \hat{g}(\kappa_x, \kappa_y, z)\, e^{j(\kappa_x x + \kappa_y y)}, \qquad (2.63)$$

where $\kappa_x = \frac{2\pi n_x}{L_x}$ and $\kappa_y = \frac{2\pi n_y}{L_y}$ are the wave-numbers, n_x and n_y are the nth Fourier mode, N_x and N_y are the total number of Fourier modes (and also grid nodes) used along each direction, in order to represent the signal, $j = \sqrt{-1}$ is the imaginary unit of the complex representation and $\hat{g}$ is a generic Fourier coefficient of the signal in modal coordinates κ_x and κ_y. The two directions are treated with a Fast Fourier Transform (FFT) algorithm imposing periodicity in lengths of L_x and L_y and projecting the signal into N_x and N_y Fourier modes in the streamwise (x) and spanwise (y). The Fourier Transform maps the variables from a uniform grid in the physical space:

$$\Delta x = \frac{N_x}{L_x},$$
$$\Delta y = \frac{N_y}{L_y}. \qquad (2.64)$$

Since the Fourier basis is orthogonal, we can calculate $\hat{g}$ in the following way:

$$\hat{g}\left(\kappa_x, \kappa_y, z\right) = \frac{1}{N_x N_y} \sum_{n_x=-\frac{N_x}{2}+1}^{\frac{N_x}{2}} \sum_{n_y=-\frac{N_y}{2}+1}^{\frac{N_y}{2}} g(x, y, z) e^{-j(\kappa_x x + \kappa_y y)}, \quad (2.65)$$

since the wall normal direction z is non homogeneous and non periodic, we proceed to adopt the Chebyshev polynomial representation along z.

We have to use the following polynomials:

$$T_{n_z}\left(z\right) = \cos\left(n_z \cos^{-1}\left(z\right)\right), \quad (2.66)$$

where $z = z^- \in [-1; 1]$ is a non-dimensional variable and the grid points coordinates along z are given by:

$$z = \cos\left(\frac{n_z \pi}{N_z}\right), \quad (2.67)$$

where N_z is the total number of modes along z. An advantage of the Chebyshev representation is that it allows a large spatial resolution close to the walls ($z = \pm 1$), where it is necessary to properly describe high velocity gradients.

The generic signal component will thus be expressed by the following Fourier-Chebyshev representation:

$$\hat{g}\left(\kappa_x, \kappa_y, z\right) = \sum_{n_z=0}^{N'_z} \hat{h}\left(\kappa_x, \kappa_y, n_z\right) T_{n_z}\left(z\right) \quad (2.68)$$

, where n_z is one of the nodes. Because of orthogonality we can also define the inverse of the Chebyshev transform:

$$\hat{h}\left(\kappa_x, \kappa_y, z\right) = \frac{2}{N_z} \sum_{n_z=0}^{N'_z} \hat{g}\left(\kappa_x, \kappa_y, n_z\right) T_{n_z}\left(z\right). \quad (2.69)$$

Finally, the three-dimensional signal representation in the spectral space is:

$$g\left(x, y, z, t\right) = \sum_{n_x=-\frac{N_x}{2}+1}^{\frac{N_x}{2}} \sum_{n_y=-\frac{N_y}{2}+1}^{\frac{N_y}{2}} \sum_{n_z=0}^{N'_z} \hat{h}\left(\kappa_x, \kappa_y, n_z, t\right) T_{n_z} e^{j(\kappa_x x + \kappa_y y)}. \quad (2.70)$$

It is important to note that the operations computed in the physical space generate aliasing, and therefore de-aliasing algorithms need to be considered, as the one presented by [98], where only two thirds of the modes are kept after the calculation of the pseudo-spectral multiplications.

2.4.4 Numerical discretization and solution of the equations

Single fluid velocity equation

The velocity equation [2.56] is represented in the following discretized form:

$$\frac{\partial}{\partial t}\left(\frac{\partial^2}{\partial z^2} - \kappa_{xy}^2\right)\hat{u}_z = \left(\frac{\partial^2}{\partial z^2} - k_{xy}^2\right)\hat{S}_z +$$

$$-\frac{\partial}{\partial z}\left(i\kappa_x\hat{S}_x + i\kappa_y\hat{S}_y + \frac{\partial\hat{S}_z}{\partial z}\right) + \qquad (2.71)$$

$$+\frac{1}{Re_\tau}\left(\frac{\partial^2}{\partial z^2} - \kappa_{xy}^2\right)\left(\frac{\partial^2}{\partial z^2} - \kappa_{xy}^2\right)\hat{w},$$

where:
$\kappa_{xy}^2 = \kappa_x^2 + \kappa_y^2$.

The eq. [2.71] above is discretized using an IMplicit-EXplicit (IMEX) scheme:

- Explicit Adam-Bashforth second order scheme for non-linear convective terms;

- Implicit Crank-Nicolson scheme for linear diffusive operators.

Considering the time steps $n-1$, n and $n+1$, we obtain:

$$\begin{cases} n-1 \implies t - \Delta t, \\ n \implies t, \\ n+1 \implies t + \Delta t. \end{cases}$$

Eq. [2.71] is then discretized on time:

$$\frac{1}{\Delta t}\left(\frac{\partial^2}{\partial z^2} - \kappa_{xy}^2\right)(\hat{w}^{n+1} - \hat{w}^n) = \frac{1}{2}\left(\frac{\partial^2}{\partial z^2} - \kappa_{xy}^2\right)\left(3\hat{S}_z^n - \hat{S}_z^{n-1}\right) +$$

$$-\frac{3}{2}\frac{\partial}{\partial z}\left(i\kappa_x\hat{S}_x^n + i\kappa_y\hat{S}_y^n + \frac{\partial\hat{S}_z^n}{\partial z}\right) +$$

$$+\frac{1}{2}\frac{\partial}{\partial z}\left(i\kappa_x\hat{S}_x^{n-1} + i\kappa_y\hat{S}_y^{n-1} + \frac{\partial\hat{S}_z^{n-1}}{\partial z}\right) + \qquad (2.72)$$

$$+\frac{1}{Re_\tau}\left(\frac{\partial^2}{\partial z^2} - \kappa_{xy}^2\right)\left(\frac{\partial^2}{\partial z^2} - \kappa_{xy}^2\right)\frac{\hat{w}^{n+1} + \hat{w}^n}{2},$$

and we introduce the coefficient:

$$\gamma = \frac{\Delta t}{2Re_\tau},$$

to obtain:

$$
\left[1 - \gamma \left(\frac{\partial^2}{\partial z^2} - \kappa_{xy}^2\right)\right] \left(\frac{\partial^2}{\partial z^2} - \kappa_{xy}^2\right) \hat{w}^{n+1} =
$$

$$
+ \frac{3\Delta t}{2} \left(\frac{\partial^2}{\partial z^2} - k_{xy}^2\right) \hat{S}_z^n - \frac{\Delta t}{2} \left(\frac{\partial^2}{\partial z^2} - \kappa_{xy}^2\right) \hat{S}_z^{n-1}
$$

$$
- \frac{3\Delta t}{2} \frac{\partial}{\partial z} \left(i\kappa_x \hat{S}_x^n + i\kappa_y \hat{S}_y^n + \frac{\partial \hat{S}_z^n}{\partial z}\right) + \tag{2.73}
$$

$$
+ \frac{\Delta t}{2} \frac{\partial}{\partial z} \left(i\kappa_x \hat{S}_x^{n-1} + i\kappa_y \hat{S}_y^{n-1} + \frac{\partial \hat{S}_z^{n-1}}{\partial z}\right) +
$$

$$
+ \left[\gamma \frac{\partial^2}{\partial z^2} + \left(1 - \kappa_{xy}^2\right)\right] \left(\frac{\partial^2}{\partial z^2} - \kappa_{xy}^2\right) \hat{w}^n.
$$

The continuity equation in its discretized form is:

$$
i\kappa_x \hat{u}^n + i\kappa_y \hat{v}^n + \frac{\partial \hat{w}^n}{\partial z} = 0. \tag{2.74}
$$

Inserting eq. [2.74] into eq. [2.73] and defining the coefficient:

$$
\lambda^2 = \frac{1 + \gamma \kappa_{xy}^2}{\gamma},
$$

we obtain:

$$
- \gamma \left(\frac{\partial^2}{\partial z^2} - \lambda^2\right) \left(\frac{\partial^2}{\partial z^2} - \kappa_{xy}^2\right) \hat{w}^{n+1} =
$$

$$
= - \kappa_{xy}^2 \left(\frac{3}{2}\hat{S}_z^n - \frac{1}{2}\hat{S}_z^{n-1}\right) \Delta t - \kappa_{xy}^2 \left[\gamma \frac{\partial^2}{\partial z^2} + \left(1 - \gamma\kappa_{xy}^2\right)\right] \hat{w}^n +
$$

$$
- \frac{\partial}{\partial z} i\kappa_x \left(\frac{3}{2}\hat{S}_x^n - \frac{1}{2}\hat{S}_x^{n-1}\right) \Delta t - \frac{\partial}{\partial z} i\kappa_x \left[\gamma \frac{\partial^2}{\partial z^2} + \left(1 - \gamma\kappa_{xy}^2\right)\right] \hat{u}^n + \tag{2.75}
$$

$$
- \frac{\partial}{\partial z} i\kappa_y \left(\frac{3}{2}\hat{S}_y^n - \frac{1}{2}\hat{S}_y^{n-1}\right) \Delta t - \frac{\partial}{\partial z} i\kappa_y \left[\gamma \frac{\partial^2}{\partial z^2} + \left(1 - \gamma\kappa_{xy}^2\right)\right] \hat{v}^n.
$$

In the following, we define the historical terms:

$$
\hat{H}_x^n = \left(\frac{3}{2}\hat{S}_x^n - \frac{1}{2}\hat{S}_x^{n-1}\right) \Delta t + \left[\gamma \frac{\partial^2}{\partial z^2} + \left(1 - \gamma\kappa_{xy}^2\right)\right] \hat{u}^n, \tag{2.76}
$$

$$
\hat{H}_y^n = \left(\frac{3}{2}\hat{S}_y^n - \frac{1}{2}\hat{S}_y^{n-1}\right) \Delta t + \left[\gamma \frac{\partial^2}{\partial z^2} + \left(1 - \gamma\kappa_{xy}^2\right)\right] \hat{v}^n, \tag{2.77}
$$

$$
\hat{H}_z^n = \left(\frac{3}{2}\hat{S}_z^n - \frac{1}{2}\hat{S}_z^{n-1}\right) \Delta t + \left[\gamma \frac{\partial^2}{\partial z^2} + \left(1 - \gamma\kappa_{xy}^2\right)\right] \hat{w}^n. \tag{2.78}
$$

Applying the terms defined in the eq. [2.76]-[2.78] into eq .[2.75]:

$$\left(\frac{\partial^2}{\partial z^2} - \lambda^2\right)\left(\frac{\partial^2}{\partial z^2} - \kappa_{xy}^2\right)\hat{u}_z^{n+1} = \frac{1}{\gamma}\kappa_{xy}^2\hat{H}_z^n +$$
$$+ \frac{1}{\gamma}\frac{\partial}{\partial z}\left(i\kappa_x\hat{H}_x^n + i\kappa_y\hat{H}_y^n\right), \tag{2.79}$$

and defining:

$$\hat{H}^n = \kappa_{xy}^2\hat{H}_z^n + \frac{\partial}{\partial z}\left(i\kappa_x\hat{H}_x^n + i\kappa_y\hat{H}_y^n\right), \tag{2.80}$$

we find the final form of the discretized equation for the velocity:

$$\left(\frac{\partial^2}{\partial z^2} - \lambda^2\right)\left(\frac{\partial^2}{\partial z^2} - \kappa_{xy}^2\right)\hat{w}^{n+1} = \frac{\hat{H}^n}{\gamma}. \tag{2.81}$$

In order to solve this 4th-order eq. [2.81], the following auxiliary variable is introduced:

$$\hat{\theta} = \left(\frac{\partial^2}{\partial z^2} - \kappa_{xy}^2\right)\hat{w}^{n+1},$$

with this, we obtain two 2nd-order equations:

$$\left(\frac{\partial^2}{\partial z^2} - \lambda^2\right)\hat{\theta} = \frac{\hat{H}^n}{\gamma}, \tag{2.82}$$

$$\left(\frac{\partial^2}{\partial z^2} - \kappa_{xy}^2\right)\hat{w}^{n+1} = \hat{\theta}. \tag{2.83}$$

The eq. [2.83] is solved using the no-slip boundary condition at the walls:

$$\begin{cases} \hat{w}^{n+1}(\pm1) = 0, \\ \dfrac{\partial\hat{w}^{n+1}}{\partial z}(\pm1) = 0. \end{cases} \tag{2.84}$$

The solution to the eq. [2.84] requires the boundary condition on $\hat{\theta}$ that is missing in the physical model. In order to avoid this problem, we rewrite $\hat{\theta}$ as follows:

$$\hat{\theta} = \hat{\theta}_1 + \hat{A}\theta_2 + \hat{B}\theta_3, \tag{2.85}$$

where $\hat{A}, \hat{B}$ are complex constants to be determined.

The components $\hat{\theta}_1$, $\hat{\theta}_2$ and $\hat{\theta}_3$, are respectively the particular and the homogeneous solution to the eq. [2.82]. These solutions are obtained from:

$$\left(\frac{\partial^2}{\partial z^2} - \lambda^2\right) = \hat{\theta}_1, \quad \hat{\theta}_1(1) = 0, \quad \hat{\theta}_1(-1) = 0, \tag{2.86}$$

$$\left(\frac{\partial^2}{\partial z^2} - \lambda^2\right) = 0, \quad \theta_2\left(1\right) = 0, \quad \theta_2\left(-1\right) = 0, \tag{2.87}$$

$$\left(\frac{\partial^2}{\partial z^2} - \lambda^2\right) = 0, \quad \theta_3\left(1\right) = 0, \quad \theta_3\left(-1\right) = 0. \tag{2.88}$$

Similarly:

$$\hat{w}^{n+1} = \hat{w}_1 + \hat{A}w_2 + \hat{B}w_3. \tag{2.89}$$

The components $\hat{w}_1$, $\hat{w}_2$ and $\hat{w}_3$, are respectively the particular and the homogeneous solution to the eq. [2.85]. These solutions are obtained from:

$$\left(\frac{\partial^2}{\partial z^2} - \kappa_{xy}^2\right)\hat{w}_1 = \hat{\theta}, \quad \hat{w}_1\left(1\right) = 0, \quad \hat{w}_1\left(-1\right) = 0, \tag{2.90}$$

$$\left(\frac{\partial^2}{\partial z^2} - \kappa_{xy}^2\right)w_2 = 0, \quad w_2\left(1\right) = 0, \quad w_2\left(-1\right) = 0, \tag{2.91}$$

$$\left(\frac{\partial^2}{\partial z^2} - \kappa_{xy}^2\right)w_3 = 0, \quad w_3\left(1\right) = 0, \quad w_3\left(-1\right) = 0. \tag{2.92}$$

The constants $\hat{A}$ and $\hat{B}$ are determined using the no-slip condition:

$$\frac{\partial \hat{w}^{n+1}}{\partial z}\left(\pm 1\right) = 0 \quad \Longrightarrow \quad \begin{cases} \dfrac{\partial \hat{w}_1}{\partial z}\left(1\right) + \hat{A}\dfrac{\partial w_2}{\partial z}\left(1\right) + \hat{B}\dfrac{\partial w_3}{\partial z}\left(1\right), \\[2ex] \dfrac{\partial \hat{w}_1}{\partial z}\left(-1\right) + \hat{A}\dfrac{\partial w_2}{\partial z}\left(-1\right) + \hat{B}\dfrac{\partial w_3}{\partial z}\left(-1\right). \end{cases}$$

The solution of equations [2.86]-[2.88] and [2.90]-[2.92] is obtained using the Gauss elimination algorithm.

Vorticity equation

The vorticity equation for the component z in the pseudo-spectral space (eq. [2.55]) becomes:

$$\left(\frac{\partial^2}{\partial z^2} - \lambda^2\right)\hat{\omega}_z^{n+1} = -\frac{1}{\gamma}\left(i\kappa_x\hat{H}_y^n - i\kappa_y\hat{H}_x^n\right). \tag{2.93}$$

The solution of the equation [2.93] is obtained with the boundary conditions:

$$\hat{\omega}_z^{n+1}\left(\pm 1\right) = i\kappa_x\hat{u}_y^{n+1} - i\kappa_y\hat{u}_x^{n+1}. \tag{2.94}$$

The solution to the equation [2.94] is obtained using the Gauss elimination algorithm.

Once $\hat{w}^{n+1}$ and $\hat{\omega}_z^{n+1}$ are determined, it is possible to determine the velocity components $\hat{u}^{n+1}$ and $\hat{v}^{n+1}$ from the spectral representation of the vorticity and the continuity equations:

$$-i\kappa_y\hat{u}^{n+1} + i\kappa_x\hat{v}^{n+1} = \hat{\omega}_z^{n+1} \tag{2.95}$$

$$-i\kappa_x \hat{u}^{n+1} - i\kappa_y \hat{v}^{n+1} = \frac{\partial \hat{w}^{n+1}}{\partial z}. \tag{2.96}$$

Cahn-Hilliard equation

Using the spectral representation, we discretize eq. [2.61] in space as follows:

$$\frac{\partial \hat{\phi}}{\partial t} = \hat{S}_\phi + s\frac{Ch^2}{Pe}\left(\frac{\partial^2}{\partial z^2} - k_{xy}^2\right)\hat{\phi} - \frac{Ch^2}{Pe}\left(\frac{\partial^2}{\partial z^2} - k_{xy}^2\right)\left(\frac{\partial^2}{\partial z^2} - k_{xy}^2\right)\hat{\phi}, \tag{2.97}$$

introducing the coefficient $\gamma_\phi = (\Delta t Ch^2)/Pe$ into the eq. [2.97]:

$$\left[\frac{1}{\gamma_\phi} - s\left(\frac{\partial^2}{\partial z^2} - k_{xy}^2\right) + \left(\frac{\partial^2}{\partial z^2} - k_{xy}^2\right)^2\right]\hat{\phi}^{n+1} = \frac{\hat{H}_\phi}{\gamma_\phi}, \tag{2.98}$$

with $\hat{H}_\phi$ as the historical term and defined as:

$$\frac{\hat{H}_\phi}{\gamma_\phi} = \frac{1}{\gamma_\phi}\left(\hat{\phi}^n + \frac{3\Delta t}{2}\hat{S}_\phi^n - \frac{\Delta t}{2}\hat{S}_\phi^{n-1}\right). \tag{2.99}$$

Decomposing the eq. [2.98] into two equivalent 2nd order equations, we get:

$$\begin{aligned}
&\left[\frac{1}{\gamma_\phi} - s\left(\frac{\partial^2}{\partial z^2} - k_{xy}^2\right) + \left(\frac{\partial^2}{\partial z^2} - k_{xy}^2\right)^2\right] = \\
&\left[\left(\frac{\partial^2}{\partial z^2} - k_{xy}^2 - \lambda_1\right)\left(\frac{\partial^2}{\partial z^2} - k_{xy}^2 - \lambda_2\right)\right],
\end{aligned} \tag{2.100}$$

where λ_1 and λ_2 are obtained from the following equation:

$$\gamma_\phi \lambda^2 - s\gamma_\phi \lambda + 1 = 0 \tag{2.101}$$

which solved for λ results into:

$$\lambda_{1,2} = \frac{s}{2} \pm \frac{\sqrt{s^2\gamma_\phi^2 - 4\gamma_\phi}}{2\gamma_\phi}. \tag{2.102}$$

Since s is inside the square root and in order to avoid imaginary solutions, there are constraints imposed to its value :

$$s \geq \sqrt{\frac{4}{\gamma}} = \sqrt{\frac{4Pe}{\Delta t Ch^2}}. \tag{2.103}$$

To ensure numerical stability, two coincident solutions are chosen $\lambda_1 = \lambda_2 = -s/2 = \sqrt{4Pe/\Delta t Ch^2}$. Assuming this, eq. [2.98] becomes:

$$\left(\frac{\partial^2}{\partial z^2} - k_{xy}^2 + \frac{s}{2} \right)^2 \hat{\phi}^{n+1} = \frac{\hat{H}_\phi}{\gamma_\phi}. \tag{2.104}$$

We introduce the variable $\theta_\phi = s\phi/2 + \Delta^2 \phi$, which helps to split the 4th order eq. [2.98] into two 2nd order equations:

$$\left(\frac{\partial^2}{\partial z^2} - \delta^2 \right) \hat{\theta}_\phi = \frac{\hat{H}_\phi}{\gamma_\phi} \tag{2.105}$$

$$\left(\frac{\partial^2}{\partial z^2} - \delta^2 \right) \hat{\phi}^{n+1} = \hat{\theta}_\phi, \tag{2.106}$$

where $\delta^2 = k_{xy}^2 - s/2$. Using the boundary conditions of neutral wettable walls and no chemical potential flux at the walls:

$$\begin{aligned} \frac{\partial \hat{\phi}^{n+1}}{\partial z}(\pm 1) &= 0 \\ \frac{\partial^3 \hat{\phi}^{n+1}}{\partial z^3}(\pm 1) &= 0 \end{aligned} \tag{2.107}$$

the boundary conditions for $\hat{\theta}$ are in the 1st and 3rd derivative, where the influence matrix method is not needed, since:

$$\frac{\partial}{\partial z}\left(\frac{\partial^2}{\partial z^2} - \delta^2 \right) \hat{\phi}^{n+1} = \frac{\partial^3 \hat{\phi}^{n+1}}{\partial z^3} = \frac{\hat{\theta}_\phi^{n+1}}{\partial z}. \tag{2.108}$$

The boundary condition to solve eq. [2.105] is then:

$$\frac{\partial \hat{\theta_\phi^{n+1}}}{\partial z}(\pm 1) = 0 \tag{2.109}$$

and the boundary condition for eq. [2.106] is:

$$\frac{\partial \hat{\phi}}{\partial z}(\pm 1) = 0 \tag{2.110}$$

As proposed in [95], the Chebyshev-Tau solution algorithm is employed to solve equations [2.105] and [2.106], and the resulting tridiagonal system of equations is solved by the Gauss elimination procedure.

2.4.5 Numerical Algorithm

The equations shown in this section are implemented in an in-house program developed by our team using the programming language Fortran. This code makes use of the Pseudo-spectral method for the discretization combined with a second-order Adam-Bashforth and Crank-Nicolson time advancement algorithm.

This code is computationally optimized using Message Passing Interface (MPI) for
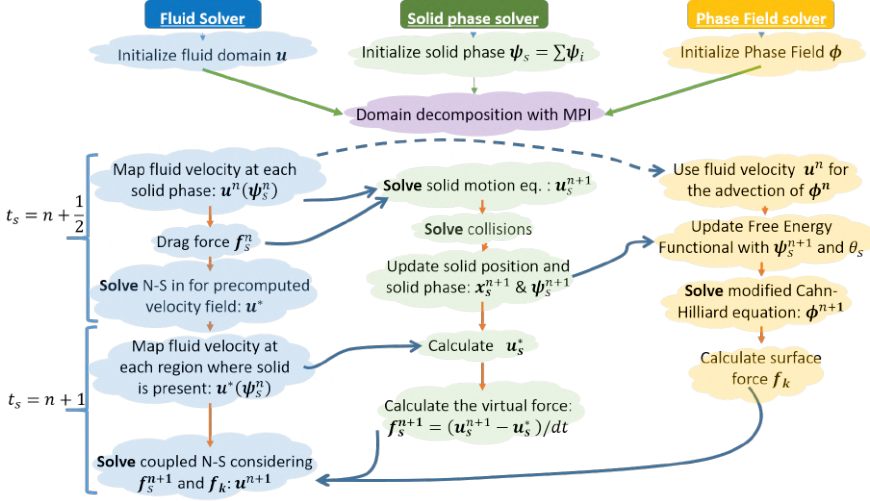
FIGURE 2.6 – Numerical algorithm flowchart constituted by three sub-solvers for the: fluid phase, drop phase and solid phase. Each time step is split into two sub-steps, an intermediate step $n/2$, where the solid phase effects are not considered to solve the N-S equations for an intermediate flow field $\mathbf{u}^*$. The final sub-step n then calculates the feedback forces from the drop and solid phases f_s and f_k respectively. Finally, they are incorporated and solved within the N-S equations, obtaining a flow field $\mathbf{u}^n$.

parallel computing. In this work, we use a domain decomposition method. If we consider the physical parameter $\psi\,(N_x \times N_y \times N_z)$, then each parallelized subdomain would have the following dimensions: $N_x \times N_{yp} \times N_{zp}$, where the subscripts yp and zp result from the division between the total number of nodes and the parallelization tasks along the direction y and z respectively.

Fig. 2.6 shows the numerical algorithm flowchart considering the interactions among the approaches involved to solve a three-phase system at one time-step (blue connections) and the sequence inside each approach solver (orange connections). The main solver is divided into three sub-solvers, one for each phase — fluid phase, drop phase and solid phase. A half-time-step correction is considered, in order to avoid any perturbation during the computation of the solid dynamics. The first half (intermediate step) $n/2$ does not consider the solid phase effects to solve the N-S equations for an intermediate flow field $\mathbf{u}^*$. The second half (final sub-step) ”n” calculates the virtual force f_s, and together with the surface tension forces f_k, it is incorporated in the N-S equations, which are solved to get a flow field $\mathbf{u}^n$ at the time level n.

3

Validation: Settling of an immersed solid in a quiescent fluid

In this chapter we present the validation and the grid sensitivity study i) for a disk settling in a 2D domain filled with a fluid and ii) for a sphere settling in a tank at different Reynolds numbers.

3.1 Settling of a 2D disk in a quiescent fluid

The numerical simulation of a disk settling in a quiescent fluid is carried out following the set up used by Glowinski et al. [99]. Initially, a disk with a radius of 1.25×10^{-3} m and a density of $\rho_s = 1250 \ kg/m^3$ is at rest and its center is located at the position of $0.04 \ m$ above the bottom of the tank ($0.02 \ m$ width and $0.06 \ m$ height), as shown in fig. 3.1.(a). The computational domain is filled up with an incompressible Newtonian fluid with a density of $\rho_f = 1000 \ kg/m^3$ and a dynamic viscosity of $\mu_f = 0.01 \ Pa \cdot s$.

The grid sensitivity is studied using three mesh qualities summarized in the table 3.1. The simulation domain has a uniform grid cell size in the horizontal axis and a Chebyshev discretization in the vertical axis. Fig. 3.2 shows that we reach the grid independence using the mesh quality 128×256.

TABLE 3.1 – Grid resolution and parameters for a settling disk simulation.

ID	Grid Resolution	Execution time per step $[s]$	Number of cores
Coarse	64×128	28×10^{-3}	8
Medium	128×256	56×10^{-3}	8
Fine	128×513	87×10^{-3}	8

The experiment begins when the disk is released from rest and it starts accelerating under the action of gravity (fig. 3.3 shows the vorticity magnitud contour for the

FIGURE 3.1 – (a) Schematic diagram of a disk settling in a 2D container. (b) Schematic diagram of a sphere settling in a tank.
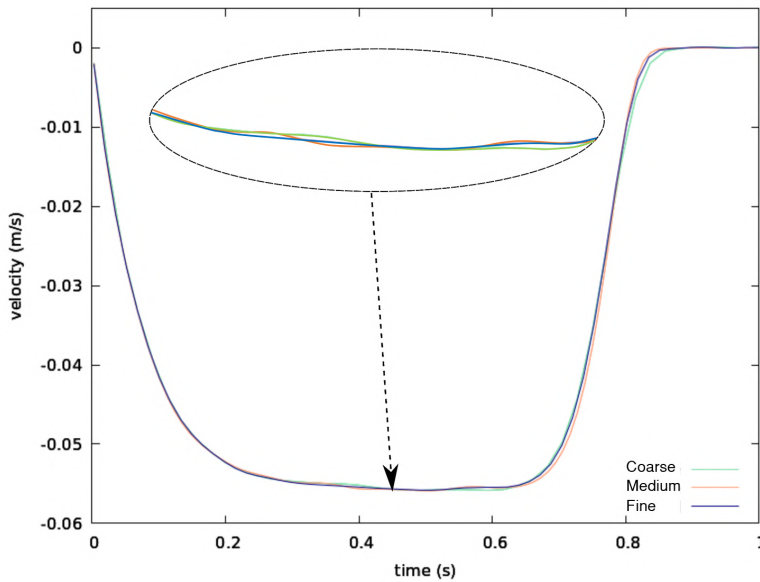
FIGURE 3.2 – Grid sensitivity of the disk velocity evolution.

settling disk at different times). The disk's velocity increases, as well as the fluid drag. After some time, gravity and drag forces are balanced, in this moment the disk reaches its terminal velocity (see fig. 3.4), remaining constant until the disk touches the bottom wall (where the collision model parameters used are $\epsilon_{pw} = 0.125$ and
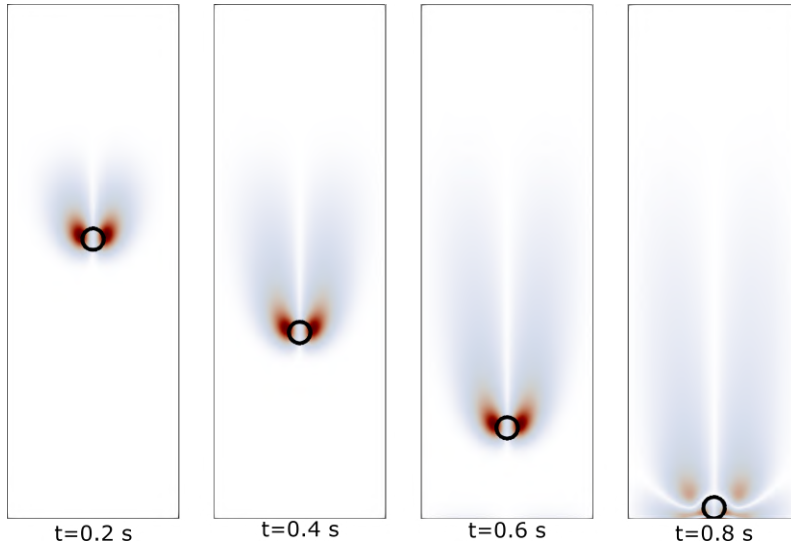
FIGURE 3.3 – Vorticity magnitude contour at different times.

$E_{pw} = 0.02$). The disk's velocity and trajectory evolution in time are reported in fig. 3.4 and 3.5 respectively. For comparison, we add the velocity curve results reached by [99, 82, 100]. Finally, we can observe that our curves are in a very good agreement with the results reached in literature, especially with Glowinski et al. [99] and Cheng-Shu et al. [82]. The latter are therefore included in our dimensionless disk position evolution plot (fig. 3.5) for comparison, where d_0 is the diameter of the disk.
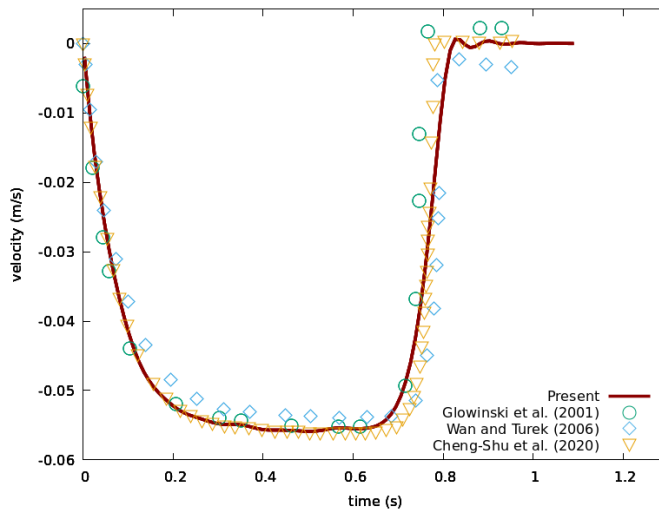
FIGURE 3.4 – Velocity evolution of the disk in time.
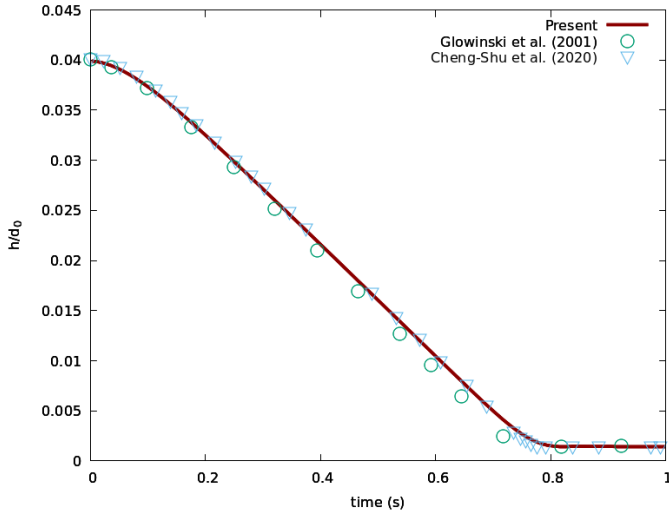
FIGURE 3.5 – Dimensionless disk position evolution in time.

3.2   Settling of a 3D sphere in a quiescent fluid

The experimental study of a sphere settling in a tank carried out by Cate et al. [101] has become a popular validation test case for simulations related to immersed rigid bodies in a fluid. Following the experimental setup, we use fluids with densities varying from 960 kg/m^3 to 970 kg/m^3 and with dynamic viscosities ranging from 0.053 $Pa \cdot s$ to 0.373 $Pa \cdot s$ (details are given in table 3.2). The 3D numerical domain consists of a tank of dimensions 0.1 m depth, 0.1 m width and 0.16 m height, where a sphere (with density $\rho_p = 1120$ kg/m^3 and diameter $d_p = d_0 = 15 \times 10^{-3}$ m) initially rests at 0.12 m from the bottom of the tank.

TABLE 3.2 – Fluid physical properties and parameters used in the simulations.

	Re	ρ_f $[kg/m^3]$	μ_f $[Pa \cdot s]$
Case 1	1.5	970	0.373
Case 2	4.1	965	0.212
Case 3	11.6	962	0.113
Case 4	32.2	960	0.058

Before running the 4 cases, a grid sensitivity test is performed to select the appropriate grid resolution. Subsequently, the parameters of "Case 3" (table 3.2) are employed, using three different resolutions: $64 \times 64 \times 256$, $64 \times 64 \times 128$ and $64 \times 64 \times 64$ cells for direction X, Y and Z respectively. Table 3.3 shows the computational details for this preliminary study, using a processor model AMD Ryzen Threadripper Pro 3995WX @ 4.2GHz.

Fig. 3.6 plots the comparison of the sphere's position evolution in time, where the increment in the mesh resolution from medium to fine is indistinguishable. Therefore, the grid quality $64 \times 64 \times 128$ is selected to perform the rest of the simulations listed in table 3.2.

TABLE 3.3 – Computational parameters used in the simulations.

ID	Grid Resolution	Execution time per step $[s]$	Number of cores
Coarse	$64 \times 64 \times 64$	80×10^{-3}	8
Medium	$64 \times 64 \times 128$	120×10^{-3}	8
Fine	$64 \times 64 \times 256$	440×10^{-3}	8
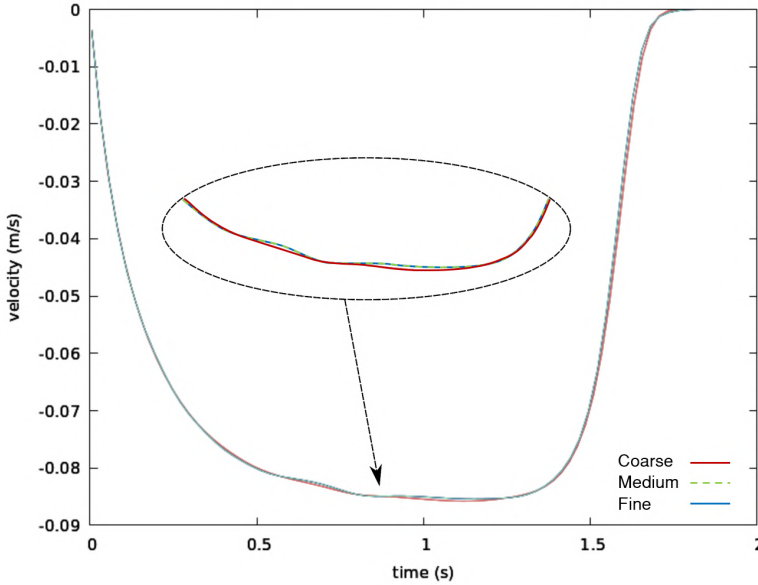
FIGURE 3.6 – Grid sensitivity using the velocity evolution of the sphere in time.

The experiment starts once the sphere is dropped. It accelerates during some time due to gravitational forces, until it reaches the terminal velocity (whose value increases as we increase the Reynolds number) (fig. 3.7). At this point, the velocity remains still in a plateau, until the sphere finally reaches the bottom of the tank. Figs. 3.7 and 3.8 depict the simulation results of the sphere velocity and the dimensionless trajectory over time (plain colored curves) and also the experimental data provided by Cate et al. [101] (represented by geometrical markers), where a very satisfactory agreement is reached for all the study cases.
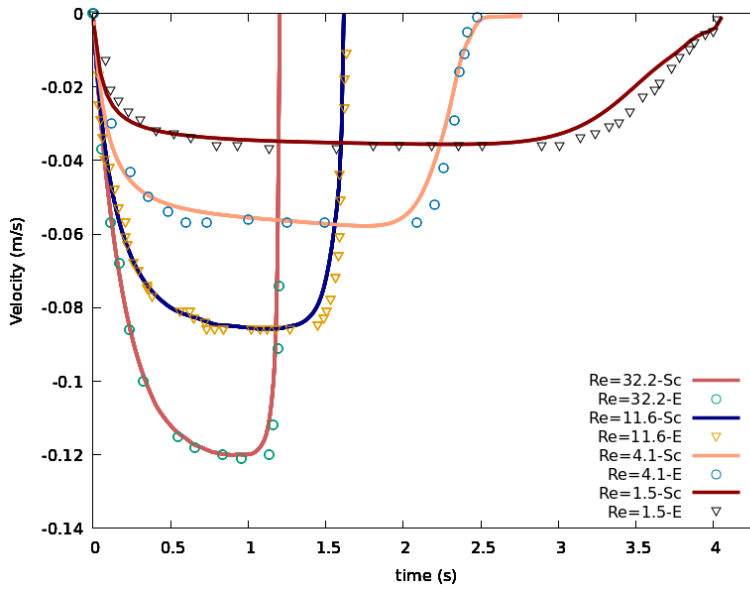
FIGURE 3.7 – Velocity evolution of the sphere in time.
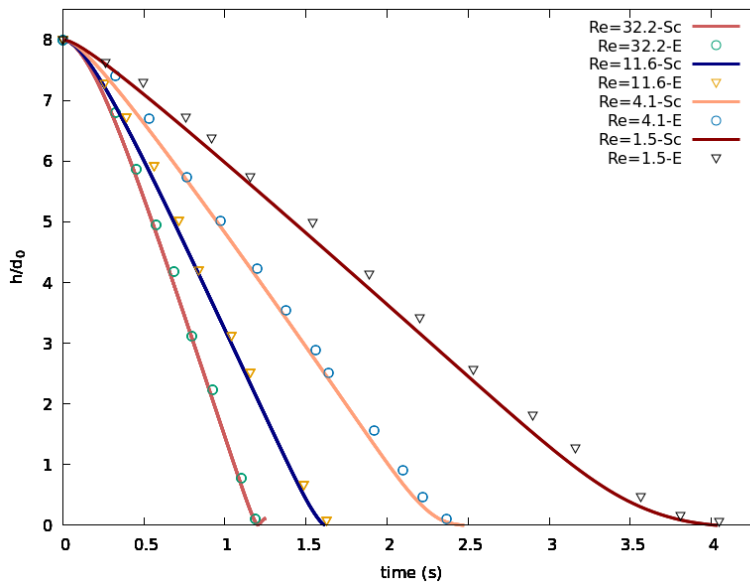
FIGURE 3.8 – Normalized position of the sphere in time.

4

Wetting effects on the interaction of an immersed solid with a binary-fluid interface

In this chapter we study the interactions between a flat binary-fluid interface and a single solid. The first part (sec. 4.1) focuses on the evolution of the contact line along the 2D cylindrical surface at different wetting conditions. The following section (sec. 4.2) presents the simulation of a heavy cylinder sinking in a binary fluid system and the last part (sec. 4.3) shows the study of the wetting effects on the submergence of a quasi-buoyant cylinder in a binary fluid domain.

4.1   Contact line equilibrium in curved surfaces

We perform the simulation of the contact line equilibrium for a cylinder in a binary fluid domain at different contact angles.
Similar to Shao et. al [60], our numerical setup consists of a squared domain of a binary fluid arranged as two horizontal layers with a cylinder fixed at the center of its interface (refer to fig. 4.1). The upper and lower boundaries are neutrally wettable walls and the left and right boundaries have a periodic boundary condition.

The cylinder has a radius of $r_{cyl} = 0.3h$ and the domain size is $2h \times 2h$ discretized with 128 grid cells along the periodic direction and with 257 grid cells in the wall normal direction. The lower fluid is set with the the phase parameter value of $\phi = 1$ and the upper one is set with $\phi = -1$. Depending on the wetting affinity preconditioned on the solid surface (eq. [2.26]), the contact line moves from the initial configuration (fig. 4.1) along the cylinder surface, until it reaches the equilibrium configuration.
A hydrophilic surface with affinity $\mathcal{X}_S = 0.35$ leads to an equilibrium contact angle $\theta_{eq} = 60°$ (panel (a) of fig. 4.2) and the contact line reaches the equilibrium above its initial vertical position (see fig. 4.3). On the other hand, the contact line moves below the initial vertical position when the solid surface is preconditioned to be hydrophobic (affinity $\mathcal{X}_S = -0.35$), leading to an equilibrium contact angle $\theta_{eq} = 120°$ (see panel (c) of fig.4.2), while a neutrally wetting surface with affinity $\mathcal{X}_S = 0$ leads to an
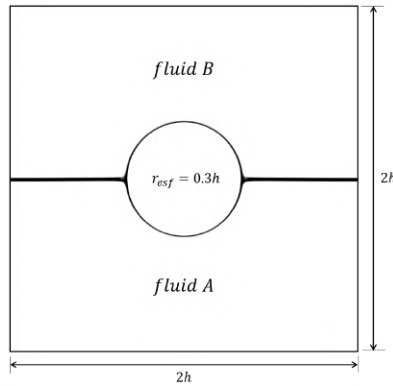
FIGURE 4.1 – Initialization setup of the simulation domain.

equilibrium contact angle $\theta_{eq} = 90°$ (panel (b) of fig. 4.2), where the interface remains flat and the contact line neither rises, nor goes below the initial position. This results match the theoretical angles predicted by eq. [2.26] and also the qualitative results obtained by other authors using different approaches [60, 52, 37].
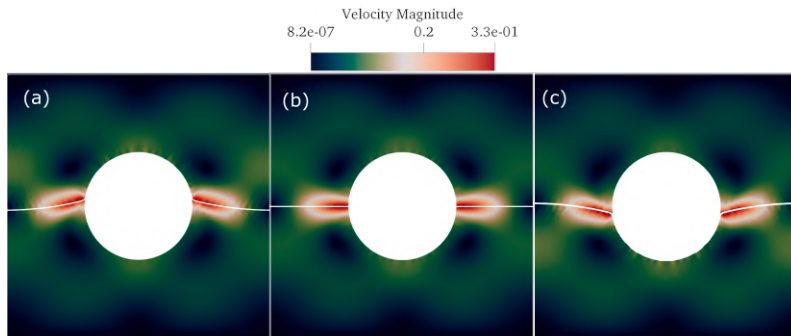
FIGURE 4.2 – (a) $\theta_{eq} = 60°$, the interface rises above the horizontal initial line. (b) $\theta_{eq} = 90°$, the interface reaches equilibrium at he same line than the initial line. (c) $\theta_{eq} = 120°$, the interface goes below the horizontal initial line. The background represents the velocity field magnitude.

4.2 Sinking of a heavy cylinder

Understanding the fluid dynamics developed by the motion of objects around a free surface is vital for some applications. In marine hydrodynamics, the wave loads produced by an immersed object motion establish the basis of marine structures design. The immersed object dynamics might trigger violent free surface motions like cavity formation, cavity collapse and free surface breakage [102]. A moving body in binary fluids is a complex scenario where the capability of numerical tools is tested in order to reproduce the fully coupled interplay of different parameters like surface tension
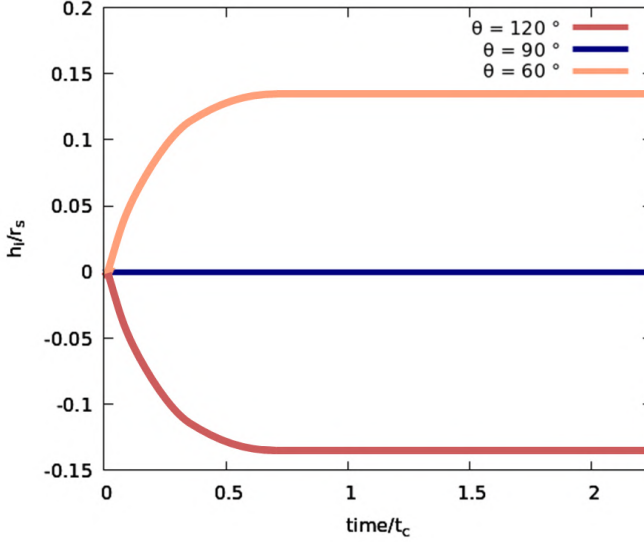
FIGURE 4.3 – Equilibrium evolution of the contact line vertical position.

forces, capillary forces, inertial forces and partial buoyancy forces (for a body migrating or trapped in between of two fluids).

In literature one can find numerical and theoretical studies of rigid-bodies motion near or through the free surface [103, 104, 51]. The one we are interested in in this section is the simulation of a heavy cylinder sinking from the free surface of a binary fluid enclosed in a 2D tank. The parameters and conditions used here are taken from the experimental study carried by Vella et al. [105].

Since the cylinder transits through two liquids, the partial buoyancy is taken into account (at each time step) through the calculation of the solid portion immersed at each fluid (Appendix A.1). The numerical domain consists of a 2D tank filled with a fluid A (density ρ_A) up to $1.4h$ from the bottom wall, while the rest is filled with a fluid B (density ρ_B) as shown in fig. 4.4, where h represents half of the height of the domain and the fluids density and dynamic viscosity ratio are $\rho_r = \rho_A/\rho_B = 833.3$ and $\eta_r = \eta_A/\eta_B = 55.6$ respectively. As a first step, a cylinder with a radius of $r_s = 0.125h$ (neglecting gravity effects) is initially placed at the interface; using a contact angle of $\theta_{eq} = 105°$, the cylinder reaches its equilibrium position at $h_0 = 0.465$ (see fig. 4.4). Then, turning on gravity effects and using a density ratio with respect to the fluid A of $\rho_s/\rho_A = 1.92$, the cylinder is released from a height of h_0 with respect to the free surface, letting the heavy cylinder sink. In order to compare with the experimental results [105], we use the characteristic time $t_c = (\sigma/\rho g^3)^{0.25}$, which is frequently used for gravity-capillary waves to travel the capillary length $l_c = (\sigma/\rho g)^{0.5}$ (the characteristic length), since the meniscus surrounding the cylinder is in hydrostatic equilibrium. We use a Reynolds number of $Re = 250$ and the Bond number is approximately equivalent to $Bo \approx (r_s/l_c)^2$. The latter value indicates that surface tension effects contribution is negligible for this experiment, and a neutral contact angle ($\theta_{eq} = 90°$) is thus assumed

for the simulations.
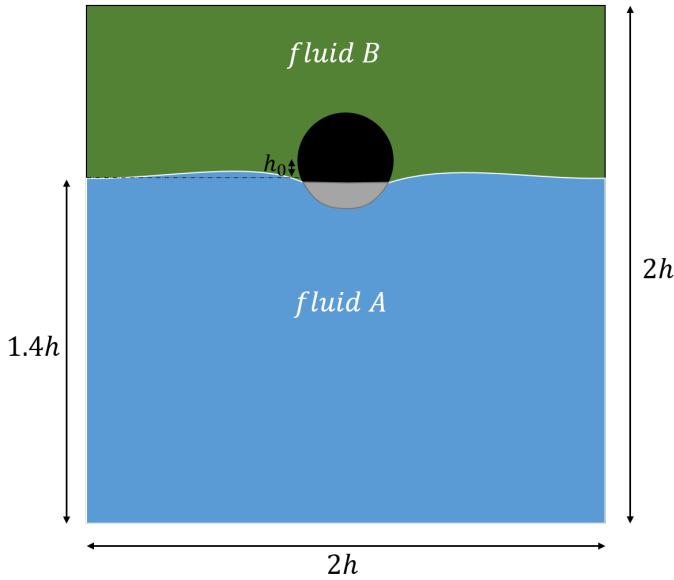
FIGURE 4.4 – Scheme of the initial set-up for a cylinder with $\rho_s = 1920 kg/m^3$ supported at an air-water free surface.

Fig. 4.5 shows a qualitative comparison of our simulations (right panel) against the experimental results (left panel), where we can observe that our simulation results are able to reproduce the main characteristic stages of the cylinder sinking experiment [105]: inflow in the region above the cylinder, cavity formation and jet generation [51].

The shape of the interface at the zone above the cylinder forms a kind of expander shape, which induces an upward jet of the fluid A and the entrainment of a portion of fluid B, attached to the cylinder surface, towards the bottom of the tank. This process is explained by fig. 4.6. Panel (a) shows that the cavity neck becomes narrow, squeezing the upper fluid out of it. The panel (b) and (c) then show how the neck walls merge, creating a pocket of upper fluid trapped and attached to the cylinder, which expands and coates the solid surface (neutral wetting), while the merged interface portion accelerates upwards, creating a bump above the free surface. When gravity and surface tension overcome the jet, the deformation is dissipated rapidly, turning the upward fluid motion into lateral waves —panel (d).

For a quantitative comparison, we plot the results of the cylinder position evolution on time (both parameters non-dimensionalized with t_c and l_c), as shown in fig. 4.7, where the numerical results, represented by a solid line, are plotted together with the experimental data [105] (represented by void circles) where a satisfactory agreement was reached.

The results obtained in this study case used a 2D domain with a periodic boundary condition in the horizontal direction and wall boundary condition in vertical direction. The grid independence test is performed to find the ideal mesh quality to efficiently reproduce experimental results. Three different mesh qualities are compared —coarse,
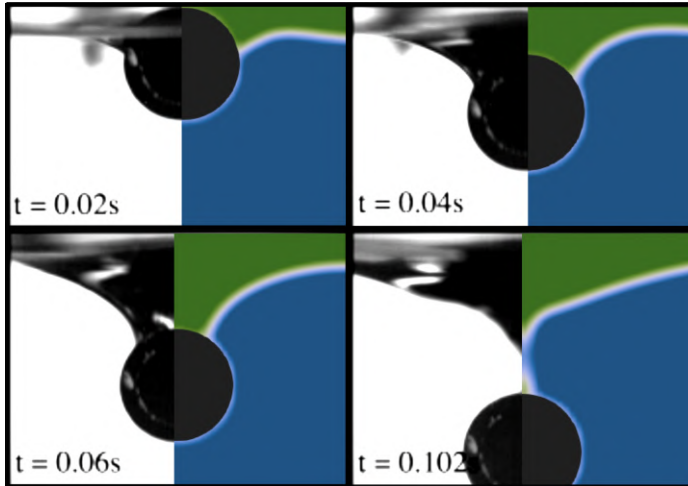
FIGURE 4.5 – Time sequence comparison of the experiment (left panel) against our simulations (right panel) for a sinking cylinder of density $1920kg/m^3$ in an binary phase system (green-blue region respectively). The cylinder is considered immersed when the cavity collapses.
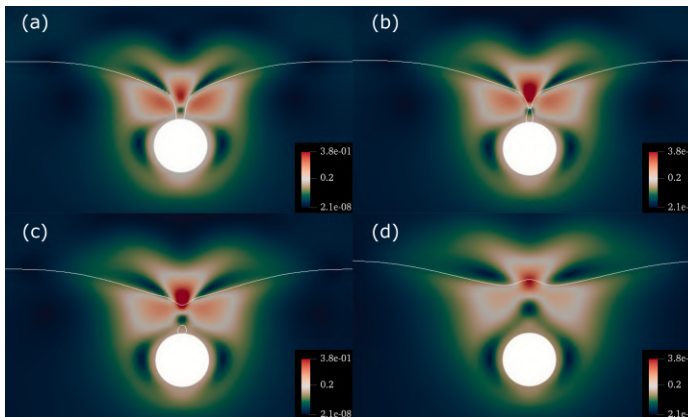
FIGURE 4.6 – Sequence of jet formation after the cavity collapse, represented with the velocity magnitude field in the background. (a) Upper fluid expelled from cavity; (b) cavity neck merged; (c) upper and lower jet formation; (d) jet rises the interface into the upper fluid.

medium and fine mesh (details can be found in table 4.1) using the processor model AMD Ryzen Threadripper Pro 3995WX @ $4.2GHz$.

Fig. 4.8 shows the result of the grid sensitivity test regarding the position evolution of the cylinder on time. We observe that the three curves overlap until time $t/t_c = 2.5$, while the buoyancy and the added mass and the viscous effects are negligible. When the cylinder starts feeling the strong change in density and viscosity, the curves take different paths. The simulations results using a medium mesh quality are indistinguishable from the one obtained using a fine mesh, this indicates that the grid independence is reached using 128×256 grid cells. Therefore, the medium mesh
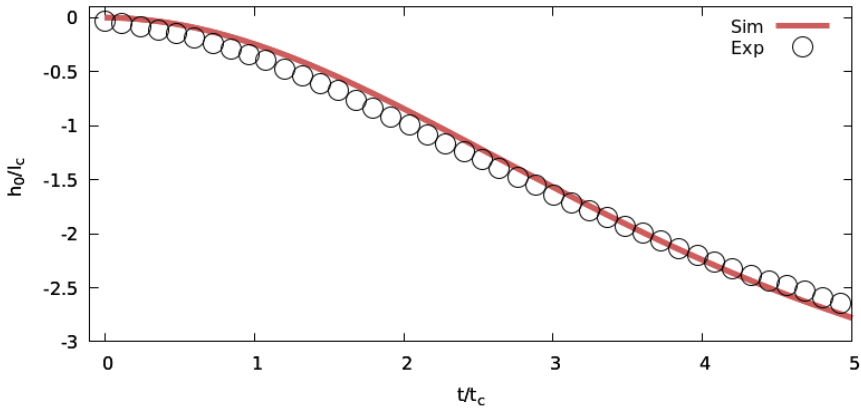
FIGURE 4.7 – Simulation results of the cylinder center position (h_0/l_c) evolution in time (t/t_c) compared with experimental data [105].

TABLE 4.1 – Parameters used in the simulations.

ID	Grid Resolution	Execution time per step $[s]$	Number of cores
Coarse	64×128	35×10^{-3}	8
Medium	128×256	100×10^{-3}	8
Fine	256×512	280×10^{-3}	8
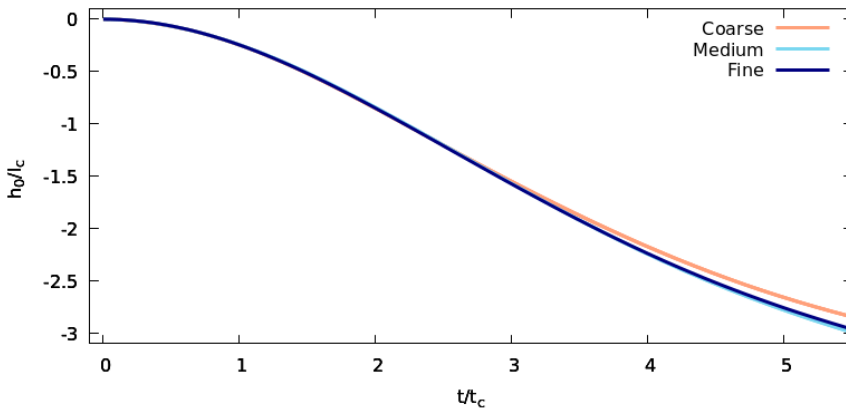
FIGURE 4.8 – Sensitivity grid resolution results of the sinking cylinder center position (h_0/l_c) evolution in time (t/t_c) using a coarse 64×128, medium 128×256 and fine 256×512 grid discretization.

quality is selected for further simulations with similar configurations.

4.3 Submergence of a light cylinder in a binary fluid domain considering surface wetting effects

Let us consider the same geometrical configuration of the 2D domain employed in sec. 4.2, where the fluid A has a density of $\rho_{fA} = 1000kg/m^3$. A cylinder (with slightly bigger density $\rho_s = 1130kg/m^3$ than fluid A) released from the rest exactly at the interface (refer to configuration (a) in fig. 4.9) would float indefinitely, because the sum of the capillary and buoyancy forces would exceed the cylinder weight [49]. In order to verify this statement, a simulation is carried out using the following parameters: fluids density ratio $\rho_r = \rho_A/\rho_B = 833.3$, fluids viscosity ratio $\eta_r = \eta_A/\eta_B = 55.6$, cylinder radius of $r_s = 0.125h$ and a neutral wettable solid surface.

The results are reported in fig. 4.10, where panel (a) shows the time sequence of the cylinder motion, and panel (b) shows its position oscillation over time, until it reaches the equilibrium and remains floating indefinitely.

(a)   (b)
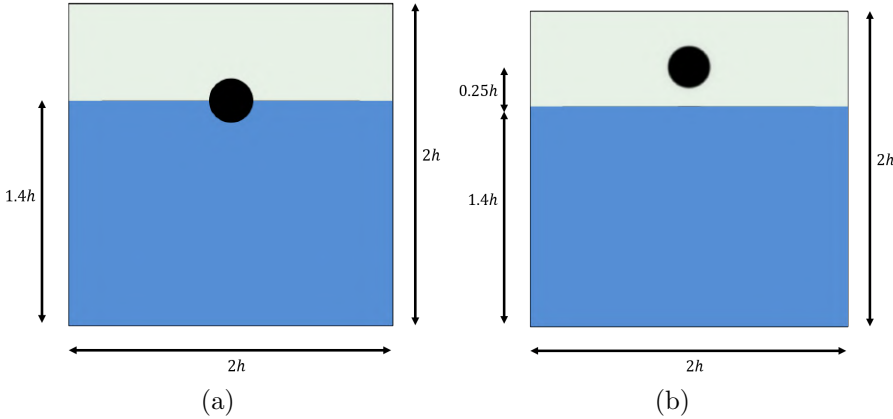
FIGURE 4.9 – (a) Initial configuration for a floating cylinder. (b) Initial configuration for a cylinder submergence by adding inertia.

In order to submerge the cylinder, we increase its inertia by releasing it from a certain height above fluid interface as shown in fig. 4.9, considering hydrophobic and hydrophilic solid surfaces. Once the solid is released, it starts accelerating because of the gravity, until it impacts with the free surface. Due to the strong contrast between fluid densities and the capillary component caused by the deflection of meniscus, the velocity then decreases.

Subsequently, the cylinder passes to the lower fluid, usually with a air bubble entrainment (remaining from the fluid B after the breakthrough), which is stuck to the upper surface of the cylinder [49].

Figures 4.11 and 4.12 show qualitatively the difference in the immersion dynamics of two identical cylinders with different wetting conditions, the first with contact angle of $\theta_{eq} = 70°$ and the second with $\theta eq = 110°$. The first characteristic that attracts our attention is that the hydrophilic cylinder reaches a deeper position in the tank, generating an upward jetting stronger than in case of the hydrophobic cylinder. We
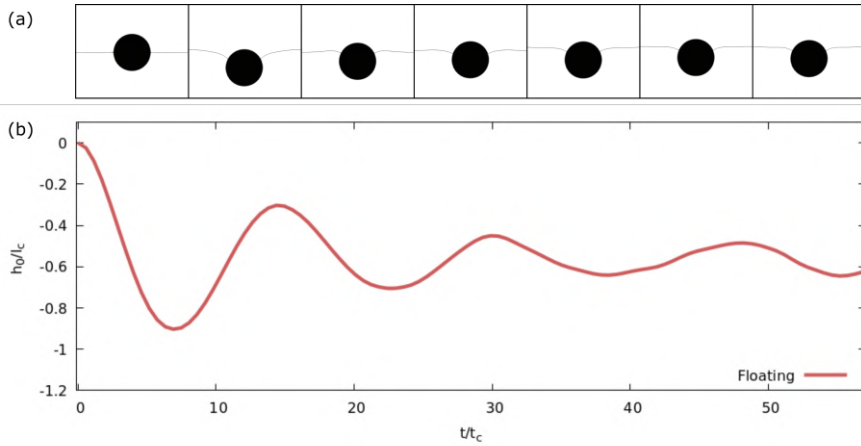
FIGURE 4.10 – (a) Contact line evolution along the simulation. (b) Equilibrium evolution plot of the center position for a floating disk initialized at the free surface.
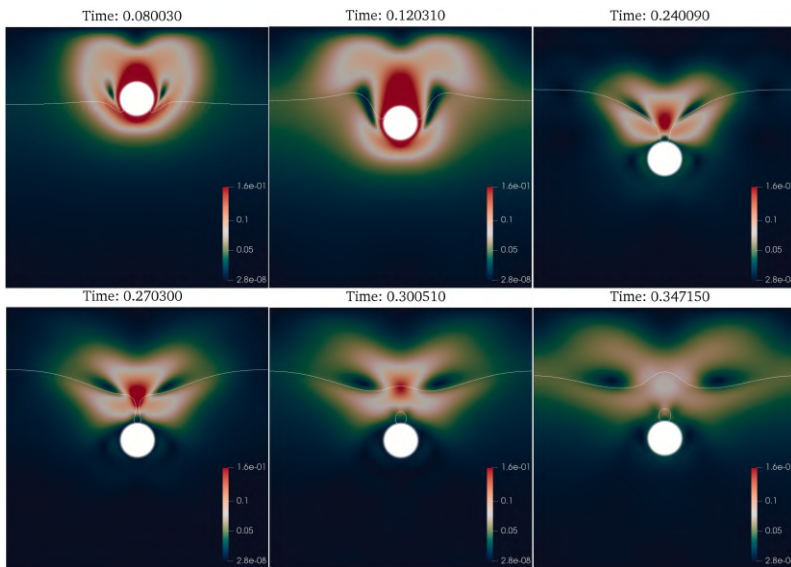
FIGURE 4.11 – Time evolution of submerging hydrophilic disk interaction with the free surface depicted over the velocity field magnitude.

can also observe how the velocity wake from the hydrophobic object is dissipated fast due to the resistance imposed by the surface tension. We may as well realize that the interface inflection due to the acute contact angle in fig. 4.11 helps with the formation of an upper fluid pocket trapped above the cylinder surface. Similar results for wetting objects sinking can be found in literature [53, 106, 107].

To further compare the wettability effects on the motion of rigid bodies entering a free surface, we plot the position evolution of the cylinder on time of both cases.
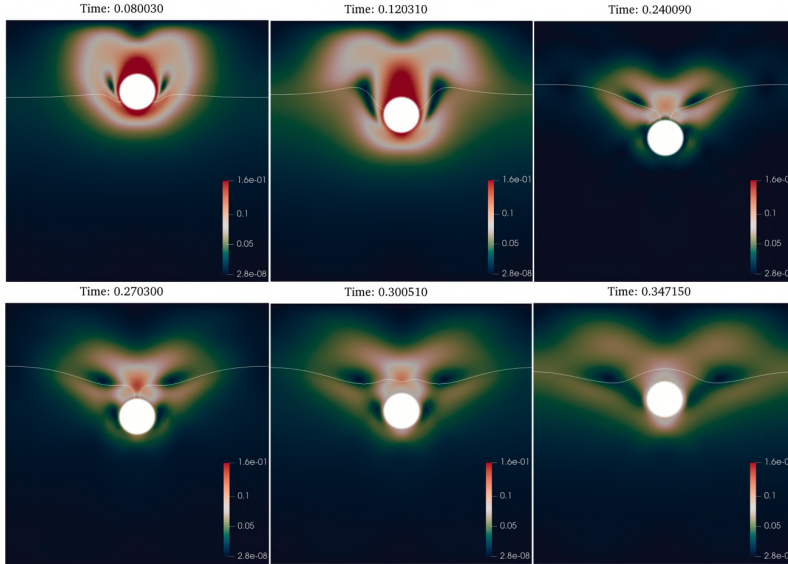
FIGURE 4.12 – Time evolution of submerging hydrophobic disk interaction with the free surface depicted over the velocity field magnitude.

(a)

(b)
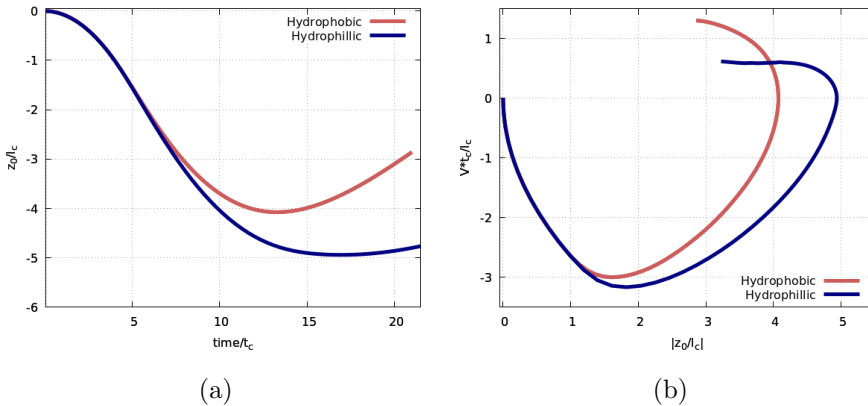
FIGURE 4.13 – (a) Evolution of the cylinder velocity against the center position. (b) Evolution of the velocity against the cylinder position.

Fig 4.13(a) shows that the hydrophilic cylinder reaches a deeper immersed position than the hydrophobic one. Fig. 4.13(b) shows that the hydrophobic solid decelerates from position z_0/l_c 1.5 to 4.1, where finally the cylinder direction of motion is flipped. These results confirm that varying the wetting conditions in the cylinder surface has important effects on the submergence dynamics and the three phase interactions. The wetting affinity of the solid surface towards one fluid will thus control the ability of the body to submerge.

5

Wetting effects on the interaction of solids and drops in three-phase systems

The type of binary fluids considered until chapter [4] were two stratified layers of fluids with an initial flat interface (free surface). In this chapter [5] we introduce a droplet as the second fluid phase immersed in a carrier fluid. In the first part, we study the evolution of the shape and position of a drop sitting on a cylindrical surface at different wetting conditions. The second part of the chapter considers two solid bodies interacting with a droplet of the same order of magnitude in a flow field. After the LBD has reached its equilibrium configuration, a shear field is initialized in the carrier flow and the LBD interactions are studied.

5.1   Solid-drop pair contact angle equilibrium

A complete work in solid-drop interactions is presented by Smith in [42], where several case studies are covered both experimentally (using one polystyrene sphere and one oil drop in an aqueous medium at different hydrophobic contact angles) and analytically (presenting equations for the prediction of the final equilibrium position for the pair in the range of 30° and 120° degrees of contact angle for various spheres-drop radius ratios). Another analytical formulation can be found in the wetting/dewetting section presented by Fakhari et al. [44], based on the premise of reaching the minimal free energy of the system by minimization of the peripheral area of a 2D drop sitting on a cylinder. These results obtained by means of the above mentioned formulation are used in the present work to validate the simulation of the dynamic contact line response to cylinder surfaces with changing wettability. Considering no gravity effects in the system during the simulations, we initialize our numerical domain by fixing a circular cylinder with radius $r_s = r_d = 0.33h$ at $0.67h$ from the lower wall. A drop with radius $r_d = 0.33h$ is placed at the center of the domain. We consider a fluid-drop density ratio of $\rho_d/\rho_f = 1000$, a viscosity ratio of $\eta_d/\eta_f = 100$ and a surface tension value of $\sigma = 0.01 N/m$.

The simulation is performed in a 2D domain with a wall boundary condition in the
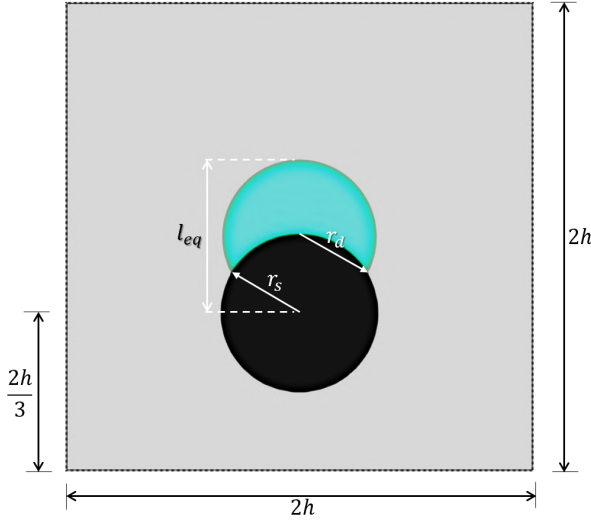
FIGURE 5.1 – Scheme of the initial configuration for the simulations.

upper and lower limits and a periodic boundary condition in the side limits. A grid sensitivity study is carried out using the parameters listed in table 5.1 to determine the optimal mesh quality for the set of simulations with different contact angle values.

TABLE 5.1 – Mesh quality list and numerical details for the simulation of the equilibrium configuration of a cylinder-drop pair.

ID	Grid Resolution	Execution time per step $[s]$	Number of cores
Coarse	64×128	28×10^{-3}	8
medium	128×256	56×10^{-3}	8
fine	256×512	87×10^{-3}	8

Fig. 5.2 shows the drop interface (iso-surface at $\phi = 0$) using different mesh qualities. One can observe as well that the grid independence is reached with 128×256 grid cells, where the difference between the drop interfaces using medium and fine mesh qualities is imperceptible.

Once the optimal mesh quality is found, a set of 7 simulations is proposed. Starting from the initial configuration presented in the initialization scheme of fig. 5.1, the system is brought to its equilibrium configuration for a range of different contact angles (from 45° to 135° as presented in [44]).

The final equilibrium configuration will be represented by the variable l_{eq}, which is defined as a distance from the center of the cylinder to the highest point of the drop (refer to fig. 5.1).

Fig 5.3(a) shows the results of the final equilibrium configuration of the cylinder-drop pair expressed in terms of l_{eq}/r_s, reported in fig 5.3(b), for each contact angle
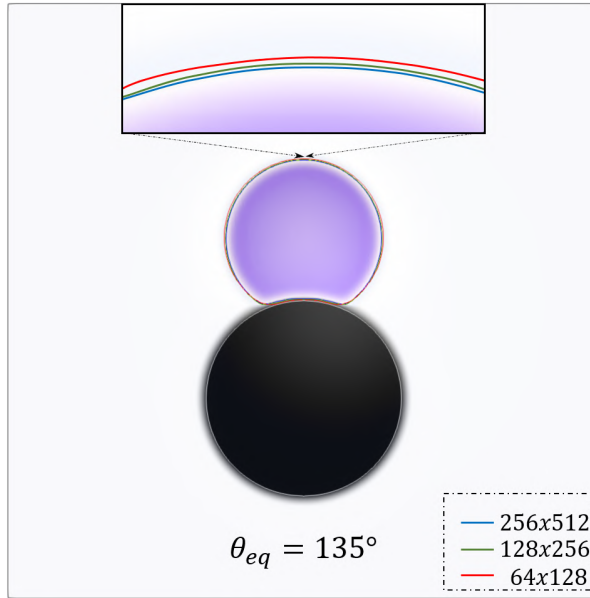
FIGURE 5.2 – Grid independence test for a drop-cylinder pair with a contact angle of 135° at equilibrium position, using: 64×128 (red line), 128×256 (green line) and 256×512 (blue line) grid cells in $y \times z$ direction respectively.
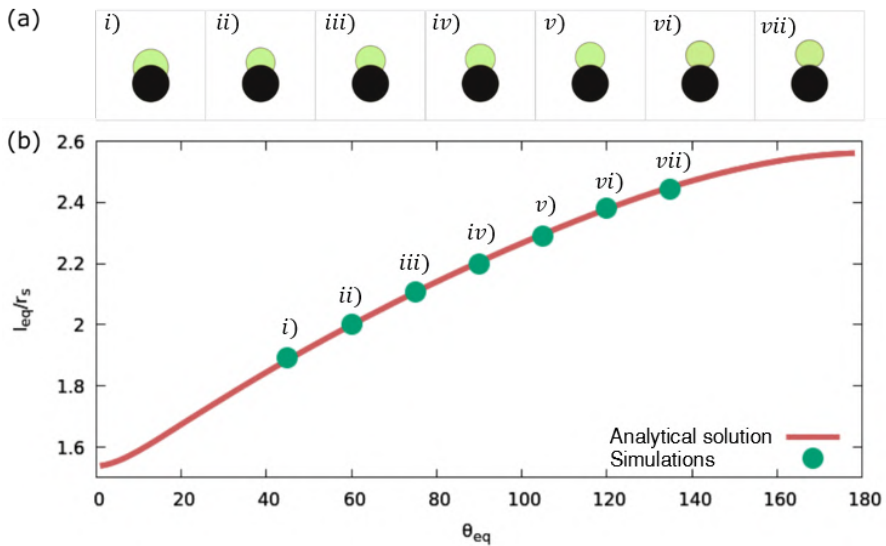
FIGURE 5.3 – (a) Cylinder-drop pair equilibrium configuration at different θ_{eq}. (b) Plot of the final configuration length l_{eq} normalized by the cylinder radius r_s for different contact angles and over the analytical curve result.

value used. Fig 5.3(b) shows the simulation results (represented by green markers) and the plot of the analytical solution (represented by the plain red curve). As illustrated in fig. 5.3, our results overlap almost perfectly over the analytical solution curve.

5.2 Liquid Bridged Doublets (LBD) in shear flow

In contrast to the above studied cases, this section includes a pair of free-moving solid bodies with active surface. They interact with a droplet in a carrier shear flow. The droplet deformation triggers the interplay between the inertial forces and the normal capillary forces, inducing the solids motion from an initial static state.
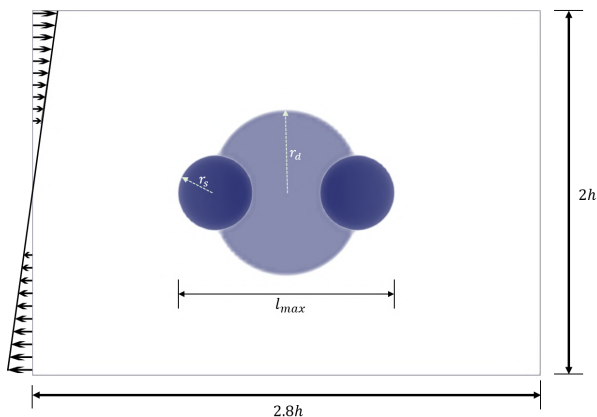
FIGURE 5.4 – Schematic of the equilibrium configuration (represented by l_{max}) of a pair of hydrophilic disks bridged by a drop, and the shear flow field (represented by arrows) on which they are initialized.

Several studies on the equilibrium configuration of bridged cylinders/spheres doublets can be found in literature [108, 109, 110]. They report analytical solutions in terms of the contact angle, the droplet volume and the maximal bridged doublet length l_{max}.

Further studies consider the interactions of a liquid bridged doublet (LBD) in a shear flow field where the drop deformation and the contact line slippage may lead to a correlated rotation of the solids around a centered axis in the drop. Experiments on the mentioned relative rotation have been performed by Smith et. al [42], where three configurations of LBD (using spheres) were presented varying the relative volume of the bridging-drop with respect to the spheres.

In this thesis — due to constraints with computational resources and time, this study has been limited to a simplified 2D numerical experiment with matched density and matched viscosity for the fluids, but the LBD geometric proportions are based on an intermediate bridging-drop volume defined in [42]. The intention of this study is to ensure the solid surface wetting parameters, the bridging-drop properties and the

shear flow field definition in order to induce a relative rotation [42].

Two identical hydrophilic ($\theta_{eq} = 73°$) disks of radius $r_s = 0.20h$ and density $\rho_s = 1120 \ kg/m^3$ bridged by a droplet (immiscible liquid) of radius $r_d = 0.43h$ and density of $\rho_d = 990 \ kg/m^3$ were initialized and brought to equilibrium by the surface forces — neglecting gravity effects, obtaining a maximal distance of $l_{max} = 1.18h$. The LBD system in equilibrium is then released in a shear flow field using a capillary number (Ca) with the value of 0.24 (fig. 5.4). This simulation is carried out using 128×128 grid nodes in the directions $y \times z$ respectively, leading to a computational time step of $t_s = 32.8 \times 10^{-3} \ sec$ using 8 cores with the processor model AMD Ryzen Threadripper Pro 3995WX @ $4.2GHz$.
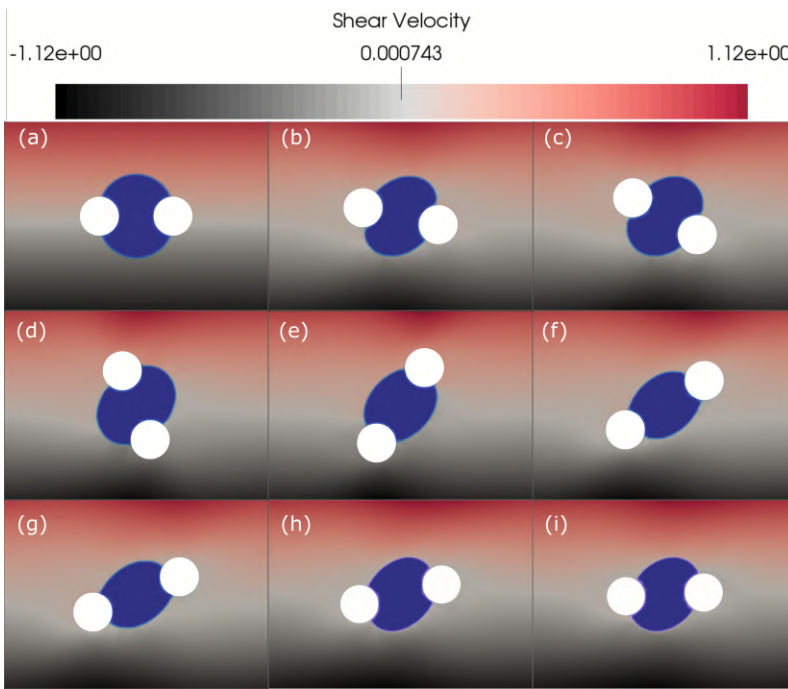
FIGURE 5.5 – Sequence of the LBD rotating in a shear flow field. (a) Equilibrium position of the LBD. (b) The drop is deformed to an elliptical shape and the disks start moving. (c), (d) The elliptical shape is kept almost invariable, but the disks circulate along the drop interface. (e) The disks reach the ellipse vertices. (f), (g) The interplay between the disks inertia and the surface tension stretches and elongates the droplet. (h) The drop adopts a more rounded shape. (i) The LBD reaches almost a mirrored version of initialization configuration.

Fig. 5.5 shows the phases of the rotation of the LBD in a shear flow field. The solid motion is started by the bridging-drop deformation into an elliptical shape as observed in panel (b) and (c), then, due to the shear field, the disks are accelerated horizontally in opposite directions, while the drop capillary forces keep them at the interface, giving them a vertical component of motion. This interplay results in a relative rotation of the disks and constant deformation in the topology of the bridging drop (since the solids

are of comparable order of magnitude with the bridging-drop). Panels (d) and (e) show the asymmetry of the rotation with respect to the vertical axis. While in the former, the bridging-drop seems to be compressed, in the latter it seems to be elongated. The LBD reaches the maximal stretch when the disks reach the ellipsoidal vertices of the bridging-drop — panel (f). There, the solid inertial forces pull the bridging-drop in the directions of the disks against the normal capillary forces. As the pair continues rotating, the capillary forces overcome the inertial ones, bringing them closer and decreasing the deformation of the bridging-drop. The rotation is symmetrical for the horizontal axis. The period of rotation of the LBD configuration is $TG = 0.28$ seconds.

6

Conclusions and future perspectives

The dynamics of the interactions between solid and binary fluid interfaces in an incompressible Newtonian fluid have been characterized using multiphase numerical techniques: the Eulerian approach for the continuous liquid phase, the Phase Field Method to describe the drop phase topology evolution and the Direct Forcing approach for the motion of solids description. A fully coupled ternary phase numerical solver was achieved by adding into the carrier liquid a surface tension term (resulting from the dynamic effects of the drop phase) and a virtual force (which plugs the effects of the solid phase dynamics in the carrier fluid), and by using a single well potential to bound the solid region in the free-energy functional of the binary fluid system.
The discretization method and numerical solution routine for the equations generated by the above mentioned approaches were developed in detail in chapter [2].

In chapter [3], the settling of an immersed solid in a quiescent fluid was investigated at different fluid properties. Two-dimensional and three-dimensional simulations were performed and satisfactorily validated with analytical and experimental data.

In chapter [4], we studied the contact line evolution in cylindrical surfaces at different wettability conditions. The results showed that the fluids interface was perturbed in different ways: climbing up the solid surface for the hydrophilic case, retreating downwards for the hydrophobic case and staying still flat for the neutrally wettable case. In the second part, we performed a simulation of the interaction between a sinking cylinder and a binary fluid interface. The simulation results matched with great accuracy the experimental data, validating the phenomena both qualitatively and quantitatively. In the last part of the section, we investigated the wetting effects on the submergence of a quasi-buoyant cylinder in a binary fluid domain. From the simulations we observed that the *capillary flotation forces* either help or resist in the submergence. For hydrophobic conditions, the solid reached shallow depths, for hydrophilic conditions, on the other hand, it sunk deeper and easier. These results are in agreement with experimental and numerical findings in literature.

The type of binary fluids considered until chapter [4] were two stratified layers of

fluids with an initial flat interface (free surface). The final part of the thesis, chapter [5], introduces a droplet as a second fluid phase. In the first part, we study the evolution of the shape and position of a drop sitting on a cylindrical surface at different wetting conditions. The resulting individual equilibrium configuration of the pair is represented by a solid-drop pair length. This length is then compared with available analytical and numerical data, to which our results match remarkably. The second part of the chapter considers two solid bodies interacting with a droplet of the same order of magnitude in a flow field. After the LBD has reached its equilibrium configuration (represented by a LBD length) in a stationary fluid, the shear flow field is initialized. The interactions within the LBD are originated by the interplay of capillary bridging forces and shear flow field effects. These interactions bring the LBD system into a relative rotation similar to the ones observed experimentally and, to the authors' knowledge, this phenomenon has not yet been addressed numerically in literature.

A limitation of this numerical implementation is that the solid sub-field must be regenerated at every time step, which increases the CPU calculation effort as we increase the number of solid particles used in the simulation; nevertheless, this limitation can be amended using optimization strategies.
The simulations of three phase interactions work in three-dimensions (3D) as fine as in 2D; some cases were tested using a 3D setup; unfortunately, meaningful results required dedication of more time and computational resources; consequently, they are not shown in this work.
The current version of the code considers the effects of the solid spheres/cylinders rotation as additional values in the solid linear velocity; thus, actual solid body rotation is not performed; however, it can be included at expenses of added computational costs.

The carried out work allows a number of potential further developments in terms of computational efficiency of the solver and of modeling capabilities of the solver.
From the point of view of the computational efficiency, the solid phase solver is currently designed to handle computations of dozens and even hundreds of solid particles in an optimal way. The parallelization strategy consists in the equitable distribution of the total number of particles tasks to be computed, among all the cores allocated for the computation. The simulation of larger amount of particles (i.e. thousands or millions) may reach a bottleneck in terms of computational speed. Therefore, for the distribution and the calculation of all the particles tasks to be computed, an optimization study using GPU parallelization is proposed instead.
From the point of view of modeling capabilities, further developments concerning non-spherical solids dynamics, big solids in drop-laden flows and lateral capillary forces in three-phase flows are suggested in the following lines.
Although it is true that for a great amount of applications, the solid bodies can be modeled as cylinders or spheres in three-phase systems, there are some others (especially for microscopic, mesoscopic and macroscopic solids) where the shape of the solids plays an important role in the dynamics of the whole system. A solid shape in the latter cases can affect several parameters directly (to mention a few: the solid rotational inertia, the after-collision bounce direction, the partial buoyancy forces and

the capillary forces). Therefore, a study of the effects of arbitrary-shaped solids on the interaction with binary fluid interfaces is encouraged.

Another topic to investigate further are the effects of considering big free moving particles in drop-laden flows. The use of small particles (point wise particles) for the stabilization of emulsions are broadly studied, especially in the cosmetic industry (due to the increasing demand of surfactant-free products). On the other hand, study results on the interaction of comparable size immersed solids and drops in drop-laden flows are still scarce. We therefore propose a study of the wettability effects on drops coalescence and breakage of big free moving particles in drop-laden flows.

Taking a closer look at the solid dynamics around the interface, we observe that the capillary forces are the main mechanisms driving the three-phase interactions. These forces are responsible for the solids self-assembly in two-dimensional structures, on the free-surface of a binary fluid system. Two solid particles attract or repel each other when their interface perturbations overlap. Although there are several numerical studies in the field, just a few of them can handle the lateral capillary forces implicitly and without an extra model. The aim of a future study would be to carry out simulations of the effects of wetting using two identical buoyant solids attached to an interface. The simulations results must be compared with the experimental data on lateral capillary forces to determine the level of accuracy of the numerical tool and decide if a model is needed.

The above mentioned capillary forces, for instance, represent in nature a mean of motility for some insects like the Pyrrhalta nymphaeae larvae. This creature has a wetting body circumscribed by a contact line (in the liquid free-surface). Therefore, in order to advance to the highest meniscus located on the edge of the liquid vessel, the insect arches its endings, perturbing the interface and forming a meniscus. These interactions generate capillary attraction forces between the insect and the edge of the vessel. Based on this real case phenomena, a study of the interaction of a simple flexible wettable membrane with the fluid-fluid interface is encouraged.

A

Appendix

A.1 Submerged solid-volume fraction

Working with a ternary phase systems implies the presence of rigid-bodies not only in one fluid, but trapped —or in the transition —between two fluids, where one must pay a special attention to the immersed volume percentage at each fluid, since the drag, added-mass and buoyancy terms of the equation of motion for solids (eq. [2.22]) depend essentially on the mass of the fluid within which they are immersed.

<div align="center">(a)   (b)</div>
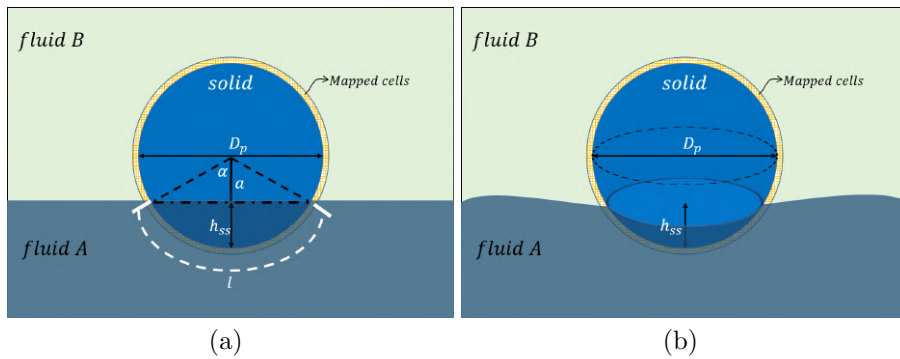
FIGURE A.1 – (a) Contact line position for a 2D solid disk partially submerged. (b) Contact line position for a 3D solid sphere partially submerged.

The contact line position helps to determine the portion of the solid at each fluid phase as depicted in fig A.1.

Since we use a diffuse interface to define the solid edge, we can map the values of ϕ on the zone delimited by the outer shell shown as a yellow region in fig. A.1, which is composed by a layer of grid-cells located right next to the solid interface (iso-surface $\psi_s = 0.5$). Subsequently, a simple algorithm detects the number of positive $Partial_A$ (fluid A) and negative $Partial_B$ (fluid B) occurrences. Knowing this and setting the fluid A as the fluid of reference, we can find the contact line position as described in the lines below.

For a 2D case, where the solid is a disk, we find the contact line position following the below procedure.

First, we calculate the portion of the circle perimeter submerged in the fluid A I_{ss}. The arc length is:

$$l = P_c I_{ss}, \tag{A.1}$$

where $P_c = \pi D_p$ is the circle perimeter. The contact line position (h_{ss}) can then be calculated using the diameter:

$$h_{ss} = 0.5 D_p - a, \tag{A.2}$$

where a is the distance from the circle center to the chord and it can be put in terms of the diameter as well:

$$a = 0.5 D_p cos\,(\alpha) \tag{A.3}$$

and by using the geometrical relationship between the circle arc and radius, we get:

$$\alpha = \frac{l}{D_p}, \tag{A.4}$$

where α is the half of the circular segment angle. Finally, putting eq. [A.4] and [A.3] into eq. [A.2], we obtain h_{ss} with respect to the bottom pole of the circle shown in fig. A.1(a):

$$h_{ss} = 0.5 D_p \left[1 - cos\,(\pi I_{ss}) \right], \tag{A.5}$$

The procedure described above can be applied to a 3D case. If we deal with a sphere, I_{ss} becomes the portion of the spherical surface area submerged in the fluid A and the value of the spherical cap is formulated as follows:

$$A_{scap} = A_{sph} I_{ss}, \tag{A.6}$$

where $A_{sph} = \pi D_p^2$ is the surface area of the sphere. The surface area of the cap in terms of the cap height is given by the following equation:

$$A_{scap} = D_p \pi h_{ss}. \tag{A.7}$$

Replacing eq. [A.7] in eq. [A.6] and isolating the contact line height h_{ss}, we obtain:

$$h_{ss} = D_p I_{ss}. \tag{A.8}$$

B

Publications, courses and projects

B.1 Referred Journals

J2 **F. K. Miranda Santa Cruz**, C. Marchioli, R. Rioboo, M. Mohaupt (2023) Experimental study on the detection of a frozen plug blockage within a Variable Conductance Heat Pipe *Appl. Therm. Eng.* (Under review)

J1 **F. K. Miranda Santa Cruz** and C. Marchioli (2023) Particle interaction with binary-fluid interfaces *J. Comput. Phys.* (In preparation)

B.2 Referred Conferences

C7 **F. K. Miranda Santa Cruz** [†],C. Marchioli , A. Hajisharifi and A. Soldati, (2022) Particle capture and trapping by large deformable drops in turbulent channel flow *APS 75th Meeting of APS, Division of Fluid Dynamics*, Indianapolis, (IN, USA).

C6 **F. K. Miranda Santa Cruz** [†], C. Marchioli, (2022) Simulation of binary-phase-fluids and wettable-rigid-bodies interactions *4th International Conference on Numerical Methods in Multiphase Flows*, Venice, (Italy).

C5 **F. K. Miranda Santa Cruz** [†], C. Marchioli, (2022) Simulation of rigid and flexible objects immersed in a fluid-drop system *6th International conference on Turbulence and Interactions*, Elba island, (Italy).

C4 **F. K. Miranda Santa Cruz** , C. Marchioli [†], A. Hajisharifi and A. Soldati , (2021) Interface topology and evolution of particle patterns on large deformable drops in turbulence *APS 74th Meeting of APS, Division of Fluid Dynamics*, Phoenix, (AZ, USA).

C3 **F. K. Miranda Santa Cruz** [†], C. Marchioli, A. Hajisharifi and A. Soldati , (2021) Particle capture by big drops in turbulent channel flow *APS 74th Meeting of APS, Division of Fluid Dynamics*, Phoenix, (AZ, USA).

C2 **F. K. Miranda Santa Cruz** [†], C. Marchioli, A. Hajisharifi and A. Soldati , (2021) Particle-droplet interaction in turbulent channel flow *IUTAM, 25th International Congress of Theoretical and Applied Mechanics*, Milan, (Italy).

C1 **F. K. Miranda Santa Cruz** [†],C. Marchioli , (2021) Simulations of rigid and flexible objects immersed in a fluid-drop system 14th *XIV Workshop in Multiphase Flows*, Gdansk, (Poland).

[†] Presentation speaker.

B.3 Advanced Courses

A9 **Convection and Deformation in Porous Media: Geophysical and Biological Flows**, International Centre for Mechanical Sciences (CISM), Udine (Italy), 2022. Coordinated by: M. De Paoli, Vienna University of Technology, Austria and C. MacMinn, University of Oxford, UK.

A8 **Complex flows and complex fluids**, International Centre for Mechanical Sciences (CISM), Udine (Italy) and JMBC,(Netherlands), 2022. Coordinated by: F. Toschi, TU Eindhoven, The Netherlands, R. Henkes, TU Delft, The Netherlands and A. Soldati, TU Wien, Austria.

A7 **Summer school in Multiphase flows**, COMETE and PAN, Gdansk, (Poland), 2021.

A6 **Physics of Granular Suspensions: Micro-Mechanics of Geophysical Flows**,International Centre for Mechanical Sciences (CISM), Udine (Italy), 2021. Coordinated by: M. Mazzuoli, University of Genova, Italy and Laurent Lacaze, IMFT-CNRS Toulouse, France.

A5 **Advances Numerical Approaches for Simulation of Turbulent Multiphase Flows**,International Centre for Mechanical Sciences (CISM) and COMETE, Udine (Italy), 2020. Coordinated by: C. Marchioli, University of Udine, Italy and Francesco Zonta, Technical University of Wien, Austria.

A4 **Collective behavior of particles in fluids**, Institut Henri Poincaré, Paris, (France), 2020.

A3 **Direct numerical simulation of solid particles, drops and bubbles in turbulence**, COMETE and TU Vienna, Vienna, (Austria), 2020.

A3 **Advanced Parallel Programming with MPI and OpenMP**, HLRS, Julich, (Germany), 2019.

A2 **Introduction to Parallel computing with MPI and OpenMP**, CINECA, Segrado, Milan, (Italy), 2019.

A1 **Advances in Dispersed Multi-Phase Flows: from Measuring to Modeling**, International Centre for Mechanical Sciences (CISM), Udine (Italy), 2020. Coordinated by: F. Coletti, University of Minnesota, Minneapolis, USA and R. Zamansky, Institut de Mécanique des Fluides, Toulouse, France.

B.4 International Projects

P1 **Freezing and defreezing experimental tests in Variable Conductance Heat Pipes**, Euro Heat Pipes (EHP), Nivelles (Belgium), 2020-2022. Supervised by: M. Mohaupt and R. Rioboo, EHP, Nivelles (Belgium).

Bibliography

[1] R. Zhao, Q. Zhang, H. Tjugito, and X. Cheng, "Raindrop impact on a sandy surface," *Physics of Fluids*, vol. 27, no. 9, p. 091111, 2015.

[2] F. Sicard and J. Toro-Mendoza, "Armored droplets as soft nanocarriers for encapsulation and release under flow conditions," *ACS nano*, vol. 15, no. 7, pp. 11 406–11 416, 2021.

[3] S. O'brien, "The meniscus near a small sphere and its relationship to line pinning of contact lines," *Journal of colloid and interface science*, vol. 183, no. 1, pp. 51–56, 1996.

[4] J. N. Israelachvili, *Intermolecular and surface forces*. Academic press, 2011.

[5] D. F. Evans and H. Wennerström, "The colloidal domain: where physics, chemistry, biology, and technology meet," 1999.

[6] D. Vella and L. Mahadevan, "The "cheerios effect"," *American journal of physics*, vol. 73, no. 9, pp. 817–825, 2005.

[7] X. Gao and L. Jiang, "Water-repellent legs of water striders," *nature*, vol. 432, no. 7013, pp. 36–36, 2004.

[8] P. A. Kralchevsky and K. Nagayama, "Capillary interactions between particles bound to interfaces, liquid films and biomembranes," *Advances in colloid and interface science*, vol. 85, no. 2-3, pp. 145–192, 2000.

[9] P. Kralchevsky and K. Nagayama, *Particles at fluid interfaces and membranes: attachment of colloid particles and proteins to interfaces and formation of two-dimensional arrays*. Elsevier, 2001.

[10] M. E. Schrader and G. I. Loeb, *Modern approaches to wettability*. Plenum New York, 1992.

[11] P.-G. De Gennes, "Wetting: statics and dynamics," *Reviews of modern physics*, vol. 57, no. 3, p. 827, 1985.

[12] P. A. Kralchevsky and K. Nagayama, "Lateral capillary forces between floating particles," in *Studies in Interface Science*. Elsevier, 2001, vol. 10, pp. 351–395.

[13] J. Sjöblom, P. Stenius, S. Simon, and B. Grimes, "Emulsion stabilization," pp. 415–454, 2013.

[14] B. Haney, D. Chen, L.-H. Cai, D. Weitz, and S. Ramakrishnan, "Millimeter-size pickering emulsions stabilized with janus microparticles," *Langmuir*, vol. 35, no. 13, pp. 4693–4701, 2019.

[15] E. Dickinson, "Food emulsions and foams: Stabilization by particles," *Current Opinion in Colloid & Interface Science*, vol. 15, no. 1-2, pp. 40–49, 2010.

[16] T. N. Hunter, R. J. Pugh, G. V. Franks, and G. J. Jameson, "The role of particles in stabilising foams and emulsions," *Advances in colloid and interface science*, vol. 137, no. 2, pp. 57–81, 2008.

[17] A. Nguyen and H. J. Schulze, *Colloidal science of flotation*. CRC Press, 2003.

[18] A. G. Atkins, T. Atkins, and M. Escudier, *A dictionary of mechanical engineering*. Oxford University Press, 2013.

[19] Y. D. Shikhmurzaev, *Capillary flows with forming interfaces*. Chapman and Hall/CRC, 2007.

[20] A. Benavides-Morán, L. Rodríguez-Jaime, and S. Laín, "Numerical investigation of the performance, hydrodynamics, and free-surface effects in unsteady flow of a horizontal axis hydrokinetic turbine," *Processes*, vol. 10, no. 1, p. 69, 2021.

[21] S. Li, A.-M. Zhang, S. Wang, and R. Han, "Transient interaction between a particle and an attached bubble with an application to cavitation in silt-laden flow," *Physics of Fluids*, vol. 30, no. 8, p. 082111, 2018.

[22] S. Dash and T. Lee, "Two spheres sedimentation dynamics in a viscous liquid column," *Computers & Fluids*, vol. 123, pp. 218–234, 2015.

[23] J. Sinclair and R. Jackson, "Gas-particle flow in a vertical pipe with particle-particle interactions," *AIChE journal*, vol. 35, no. 9, pp. 1473–1486, 1989.

[24] S. Chen and G. D. Doolen, "Lattice boltzmann method for fluid flows," *Annual review of fluid mechanics*, vol. 30, no. 1, pp. 329–364, 1998.

[25] C. K. Aidun, Y. Lu, and E.-J. Ding, "Direct analysis of particulate suspensions with inertia using the discrete boltzmann equation," *Journal of Fluid Mechanics*, vol. 373, pp. 287–311, 1998.

[26] B. Yang, S. Chen, and K. Liu, "Direct numerical simulations of particle sedimentation with heat transfer using the lattice boltzmann method," *International Journal of Heat and Mass Transfer*, vol. 104, pp. 419–437, 2017.

[27] K. Stratford and I. Pagonabarraga, "Parallel simulation of particle suspensions with the lattice boltzmann method," *Computers & Mathematics with Applications*, vol. 55, no. 7, pp. 1585–1593, 2008.

[28] T. Kempe and J. Fröhlich, "An improved immersed boundary method with direct forcing for the simulation of particle laden flows," *Journal of Computational Physics*, vol. 231, no. 9, pp. 3663–3684, 2012.

[29] W.-P. Breugem, "A second-order accurate immersed boundary method for fully resolved simulations of particle-laden flows," *Journal of Computational Physics*, vol. 231, no. 13, pp. 4469–4498, 2012.

[30] ——, "A combined soft-sphere collision/immersed boundary method for resolved simulations of particulate flows," in *Fluids Engineering Division Summer Meeting*, vol. 49484, 2010, pp. 2381–2392.

[31] M. Jiang and Z. Liu, "A boundary thickening-based direct forcing immersed boundary method for fully resolved simulation of particle-laden flows," *Journal of Computational Physics*, vol. 390, pp. 203–231, 2019.

[32] K. Luo, Z. Wang, J. Tan, and J. Fan, "An improved direct-forcing immersed boundary method with inward retraction of lagrangian points for simulation of particle-laden flows," *Journal of Computational Physics*, vol. 376, pp. 210–227, 2019.

[33] R. Glowinski, T.-W. Pan, T. I. Hesla, and D. D. Joseph, "A distributed lagrange multiplier/fictitious domain method for particulate flows," *International Journal of Multiphase Flow*, vol. 25, no. 5, pp. 755–794, 1999.

[34] C.-Y. Zhang, H. Ding, P. Gao, and Y.-L. Wu, "Diffuse interface simulation of ternary fluids in contact with solid," *Journal of Computational Physics*, vol. 309, pp. 37–51, 2016.

[35] R. Yamamoto, J. J. Molina, and Y. Nakayama, "Smoothed profile method for direct numerical simulations of hydrodynamically interacting particles," *Soft Matter*, vol. 17, no. 16, pp. 4226–4253, 2021.

[36] M. Reder, D. Schneider, F. Wang, S. Daubner, and B. Nestler, "Phase-field formulation of a fictitious domain method for particulate flows interacting with complex and evolving geometries," *International Journal for Numerical Methods in Fluids*, vol. 93, no. 8, pp. 2486–2507, 2021.

[37] B. Yang and S. Chen, "Simulation of interaction between a freely moving solid particle and a freely moving liquid droplet by lattice boltzmann method," *International Journal of Heat and Mass Transfer*, vol. 127, pp. 474–484, 2018.

[38] M. D. Saroka and N. Ashgriz, "Separation criteria for off-axis binary drop collisions," *Journal of Fluids*, vol. 2015, 2015.

[39] P. O'rourke, "Modelling of drop interactions in thick sprays and a comparison with experiments," *I. Mech. E., C*, vol. 404, no. 80, pp. 101–116, 1980.

[40] T. Inamuro, R. Tomita, and F. Ogino, "Lattice boltzmann simulations of drop deformation and breakup in shear flows," *International Journal of Modern Physics B*, vol. 17, no. 01n02, pp. 21–26, 2003.

[41] S. Elghobashi, "Direct numerical simulation of turbulent flows laden with droplets or bubbles," *Annual Review of Fluid Mechanics*, vol. 51, no. 1, pp. 217–244, 2019.

[42] P. Smith and T. Van de Ven, "Interactions between drops and particles in simple shear," *Colloids and surfaces*, vol. 15, pp. 211–231, 1985.

[43] M. Long, J. Hasanyan, and S. Jung, "Spreading dynamics of a droplet impacting a sphere," *Physics of Fluids*, vol. 34, no. 10, p. 102115, 2022.

[44] A. Fakhari and D. Bolster, "Diffuse interface modeling of three-phase contact line dynamics on curved boundaries: A lattice boltzmann model for large density and viscosity ratios," *Journal of Computational Physics*, vol. 334, pp. 620–638, 2017.

[45] S. Banitabaei and A. Amirfazli, "Droplet impact onto a solid sphere: Effect of wettability and impact velocity," *Physics of Fluids*, vol. 29, no. 6, p. 062111, 2017.

[46] N. Arai, S. Watanabe, M. T. Miyahara, R. Yamamoto, U. Hampel, and G. Lecrivain, "Direct observation of the attachment behavior of hydrophobic colloidal particles onto a bubble surface," *Soft matter*, vol. 16, no. 3, pp. 695–702, 2020.

[47] Z. Brabcová, T. Karapantsios, M. Kostoglou, P. Basařová, and K. Matis, "Bubble–particle collision interaction in flotation systems," *Colloids and Surfaces A: Physicochemical and Engineering Aspects*, vol. 473, pp. 95–103, 2015.

[48] C. Gu and L. Botto, "Fipi: A fast numerical method for the simulation of particle-laden fluid interfaces," *Computer Physics Communications*, vol. 256, p. 107447, 2020.

[49] J.-L. Pierson and J. Magnaudet, "Inertial settling of a sphere through an interface. part 2. sphere and tail dynamics," *Journal of Fluid Mechanics*, vol. 835, pp. 808–851, 2018.

[50] R. Di Mundo, F. Bottiglione, G. Pascazio, and G. Carbone, "Water entry and fall of hydrophobic and superhydrophobic teflon spheres," *Journal of Physics: Condensed Matter*, vol. 30, no. 44, p. 445001, 2018.

[51] M. Greenhow, "Water-entry and-exit of a horizontal circular cylinder," *Applied Ocean Research*, vol. 10, no. 4, pp. 191–198, 1988.

[52] Z. Li, J. Favier, U. D'Ortona, and S. Poncet, "An immersed boundary-lattice boltzmann method for single-and multi-component fluid flows," *Journal of Computational Physics*, vol. 304, pp. 424–440, 2016.

[53] M. Reder, P. W. Hoffrogge, D. Schneider, and B. Nestler, "A phase-field based model for coupling two-phase flow with the motion of immersed rigid bodies," *International Journal for Numerical Methods in Engineering*, 2022.

[54] A. S. Joshi and Y. Sun, "Multiphase lattice boltzmann method for particle suspensions," *Physical Review E*, vol. 79, no. 6, p. 066703, 2009.

[55] H. Shinto, "Computer simulation of wetting, capillary forces, and particle-stabilized emulsions: From molecular-scale to mesoscale modeling," *Advanced Powder Technology*, vol. 23, no. 5, pp. 538–547, 2012.

[56] M. Chen, K. Kontomaris, and J. McLaughlin, "Direct numerical simulation of droplet collisions in a turbulent channel flow. part i: collision algorithm," *International Journal of Multiphase Flow*, vol. 24, no. 7, pp. 1079–1103, 1999.

[57] R. Guillaument, S. Vincent, and J.-P. Caltagirone, "An original algorithm for vof based method to handle wetting effect in multiphase flow simulation," *Mechanics Research Communications*, vol. 63, pp. 26–32, 2015.

[58] L. Scarbolo, F. Bianco, and A. Soldati, "Coalescence and breakup of large droplets in turbulent channel flow," *Physics of Fluids*, vol. 27, no. 7, p. 073302, 2015.

[59] B. Chen, G. Li, W. Wang, and P. Wang, "3d numerical simulation of droplet passive breakup in a micro-channel t-junction using the volume-of-fluid method," *Applied Thermal Engineering*, vol. 88, pp. 94–101, 2015.

[60] J. Shao, C. Shu, and Y.-T. Chew, "Development of an immersed boundary-phase field-lattice boltzmann method for neumann boundary condition to study contact line dynamics," *Journal of Computational Physics*, vol. 234, pp. 8–32, 2013.

[61] D. Iwahara, H. Shinto, M. Miyahara, and K. Higashitani, "Liquid drops on homogeneous and chemically heterogeneous surfaces: A two-dimensional lattice boltzmann study," *Langmuir*, vol. 19, no. 21, pp. 9086–9093, 2003.

[62] J. Yang, J. Wang, and J. Kim, "Energy-stable method for the cahn–hilliard equation in arbitrary domains," *International Journal of Mechanical Sciences*, vol. 228, p. 107489, 2022.

[63] B. Bunner and G. Tryggvason, "Direct numerical simulations of three-dimensional bubbly flows," *Physics of Fluids*, vol. 11, no. 8, pp. 1967–1969, 1999.

[64] G. Tryggvason, B. Bunner, A. Esmaeeli, D. Juric, N. Al-Rawahi, W. Tauber, J. Han, S. Nas, and Y.-J. Jan, "A front-tracking method for the computations of multiphase flow," *Journal of computational physics*, vol. 169, no. 2, pp. 708–759, 2001.

[65] S. O. Unverdi and G. Tryggvason, "A front-tracking method for viscous, incompressible, multi-fluid flows," *Journal of computational physics*, vol. 100, no. 1, pp. 25–37, 1992.

[66] A. Prosperetti and G. Tryggvason, *Computational methods for multiphase flow*. Cambridge university press, 2009.

[67] C. W. Hirt and B. D. Nichols, "Volume of fluid (vof) method for the dynamics of free boundaries," *Journal of computational physics*, vol. 39, no. 1, pp. 201–225, 1981.

[68] D. Gueyffier, J. Li, A. Nadim, R. Scardovelli, and S. Zaleski, "Volume-of-fluid interface tracking with smoothed surface stress methods for three-dimensional flows," *Journal of Computational physics*, vol. 152, no. 2, pp. 423–456, 1999.

[69] R. Scardovelli and S. Zaleski, "Direct numerical simulation of free-surface and interfacial flow," *Annual review of fluid mechanics*, vol. 31, no. 1, pp. 567–603, 1999.

[70] S. Osher and J. A. Sethian, "Fronts propagating with curvature-dependent speed: Algorithms based on hamilton-jacobi formulations," *Journal of computational physics*, vol. 79, no. 1, pp. 12–49, 1988.

[71] M. Sussman, P. Smereka, and S. Osher, "A level set approach for computing solutions to incompressible two-phase flow," *Journal of Computational physics*, vol. 114, no. 1, pp. 146–159, 1994.

[72] T. Ménard, S. Tanguy, and A. Berlemont, "Coupling level set/vof/ghost fluid methods: Validation and application to 3d simulation of the primary break-up of a liquid jet," *International Journal of Multiphase Flow*, vol. 33, no. 5, pp. 510–524, 2007.

[73] O. Desjardins, V. Moureau, and H. Pitsch, "An accurate conservative level set/ghost fluid method for simulating turbulent atomization," *Journal of computational physics*, vol. 227, no. 18, pp. 8395–8416, 2008.

[74] J. W. Cahn and J. E. Hilliard, "Free energy of a nonuniform system. i. interfacial free energy," *The Journal of chemical physics*, vol. 28, no. 2, pp. 258–267, 1958.

[75] J. W. Cahn, "Free energy of a nonuniform system. ii. thermodynamic basis," *The Journal of chemical physics*, vol. 30, no. 5, pp. 1121–1124, 1959.

[76] J. W. Cahn and J. E. Hilliard, "Free energy of a nonuniform system. iii. nucleation in a two-component incompressible fluid," *The Journal of chemical physics*, vol. 31, no. 3, pp. 688–699, 1959.

[77] D. M. Anderson, G. B. McFadden, and A. A. Wheeler, "Diffuse-interface methods in fluid mechanics," Tech. Rep., 1997.

[78] D. Jacqmin, "Calculation of two-phase navier–stokes flows using phase-field modeling," *Journal of computational physics*, vol. 155, no. 1, pp. 96–127, 1999.

[79] V. E. Badalassi, H. D. Ceniceros, and S. Banerjee, "Computation of multiphase systems with phase field models," *Journal of computational physics*, vol. 190, no. 2, pp. 371–397, 2003.

[80] H. Ding and C.-j. Yuan, "On the diffuse interface method using a dual-resolution cartesian grid," *Journal of Computational Physics*, vol. 273, pp. 243–254, 2014.

[81] P. Yue, C. Zhou, and J. J. Feng, "Spontaneous shrinkage of drops and mass conservation in phase-field simulations," *Journal of Computational Physics*, vol. 223, no. 1, pp. 1–9, 2007.

[82] C.-S. You, M.-J. Chern, D. Z. Noor, and T.-L. Horng, "Numerical investigation of freely falling objects using direct-forcing immersed boundary method," *Mathematics*, vol. 8, no. 9, p. 1619, 2020.

[83] H. Tanaka and T. Araki, "Simulation method of colloidal suspensions with hydrodynamic interactions: Fluid particle dynamics," *Physical review letters*, vol. 85, no. 6, p. 1338, 2000.

[84] Y. Nakayama and R. Yamamoto, "Simulation method to resolve hydrodynamic interactions in colloidal dispersions," *Physical Review E*, vol. 71, no. 3, p. 036707, 2005.

[85] D. Z. Noor, M.-J. Chern, and T.-L. Horng, "An immersed boundary method to solve fluid–solid interaction problems," *Computational Mechanics*, vol. 44, no. 4, pp. 447–453, 2009.

[86] M.-J. Chern, D. Z. Noor, C.-B. Liao, and T.-L. Horng, "Direct-forcing immersed boundary method for mixed heat transfer," *Communications in Computational Physics*, vol. 18, no. 4, pp. 1072–1094, 2015.

[87] T.-L. Horng, P.-W. Hsieh, S.-Y. Yang, and C.-S. You, "A simple direct-forcing immersed boundary projection method with prediction-correction for fluid-solid interaction problems," *Computers & Fluids*, vol. 176, pp. 135–152, 2018.

[88] B. Bigot, T. Bonometti, L. Lacaze, and O. Thual, "A simple immersed-boundary method for solid–fluid interaction in constant-and stratified-density flows," *Computers & Fluids*, vol. 97, pp. 126–142, 2014.

[89] Z.-G. Feng and E. E. Michaelides, "Proteus: a direct forcing method in the simulations of particulate flows," *Journal of Computational Physics*, vol. 202, no. 1, pp. 20–51, 2005.

[90] J. W. Cahn, "Critical point wetting," *The Journal of Chemical Physics*, vol. 66, no. 8, pp. 3667–3672, 1977.

[91] C. E. Weatherburn, *Differential geometry of three dimensions*. Cambridge University Press, 2016, vol. 1.

[92] G. K. Batchelor, *An introduction to fluid dynamics*. Cambridge university press, 2000.

[93] F. Magaletti, F. Picano, M. Chinappi, L. Marino, and C. M. Casciola, "The sharp-interface limit of the cahn–hilliard/navier–stokes model for binary fluids," *Journal of Fluid Mechanics*, vol. 714, pp. 95–126, 2013.

[94] G. Soligo, A. Roccon, and A. Soldati, "Mass-conservation-improved phase field methods for turbulent multiphase flow simulation," *Acta Mechanica*, vol. 230, no. 2, pp. 683–696, 2019.

[95] J. Kim, P. Moin, and R. Moser, "Turbulence statistics in fully developed channel flow at low reynolds number," *Journal of fluid mechanics*, vol. 177, pp. 133–166, 1987.

[96] P. Yue, J. J. Feng, C. Liu, and J. Shen, "A diffuse-interface method for simulating two-phase flows of complex fluids," *Journal of Fluid Mechanics*, vol. 515, pp. 293–317, 2004.

[97] A. Lamorgese and R. Mauri, "Diffuse-interface modeling of phase segregation in liquid mixtures," *International journal of multiphase flow*, vol. 34, no. 10, pp. 987–995, 2008.

[98] J. P. Boyd, *Chebyshev and Fourier spectral methods*. Courier Corporation, 2001.

[99] R. Glowinski, T.-W. Pan, T. I. Hesla, D. D. Joseph, and J. Periaux, "A fictitious domain approach to the direct numerical simulation of incompressible viscous flow past moving rigid bodies: application to particulate flow," *Journal of computational physics*, vol. 169, no. 2, pp. 363–426, 2001.

[100] D. Wan and S. Turek, "Direct numerical simulation of particulate flow via multigrid fem techniques and the fictitious boundary method," *International Journal for Numerical Methods in Fluids*, vol. 51, no. 5, pp. 531–566, 2006.

[101] A. Ten Cate, C. Nieuwstad, J. Derksen, and H. Van den Akker, "Particle imaging velocimetry experiments and lattice-boltzmann simulations on a single sphere settling under gravity," *Physics of Fluids*, vol. 14, no. 11, pp. 4012–4025, 2002.

[102] S. Moyo and M. Greenhow, "Free motion of a cylinder moving below and through a free surface," *Applied Ocean Research*, vol. 22, no. 1, pp. 31–44, 2000.

[103] P. Lin, "A fixed-grid model for simulation of a moving body in free surface flows," *Computers & fluids*, vol. 36, no. 3, pp. 549–561, 2007.

[104] P. A. Tyvand and T. Miloh, "Free-surface flow due to impulsive motion of a submerged circular cylinder," *Journal of Fluid Mechanics*, vol. 286, pp. 67–101, 1995.

[105] D. Vella, D.-G. Lee, and H.-Y. Kim, "Sinking of a horizontal cylinder," *Langmuir*, vol. 22, no. 7, pp. 2972–2974, 2006.

[106] S. Yi, "A phase field method for the numerical simulation of rigid particulate in two-phase flows," *Fluid Dynamics Research*, vol. 52, no. 1, p. 015512, 2020.

[107] J. M. Aristoff and J. W. Bush, "Water entry of small hydrophobic spheres," *Journal of Fluid Mechanics*, vol. 619, pp. 45–78, 2009.

[108] M. A. Erle, D. Dyson, and N. R. Morrow, "Liquid bridges between cylinders, in a torus, and between spheres," *AIChE Journal*, vol. 17, no. 1, pp. 115–121, 1971.

[109] F. Orr, L. Scriven, and A. P. Rivas, "Pendular rings between solids: meniscus properties and capillary force," *Journal of Fluid Mechanics*, vol. 67, no. 4, pp. 723–742, 1975.

[110] C. D. Willett, M. J. Adams, S. A. Johnson, and J. P. Seville, "Capillary bridges between two spherical bodies," *Langmuir*, vol. 16, no. 24, pp. 9396–9405, 2000.